Accepted Manuscript

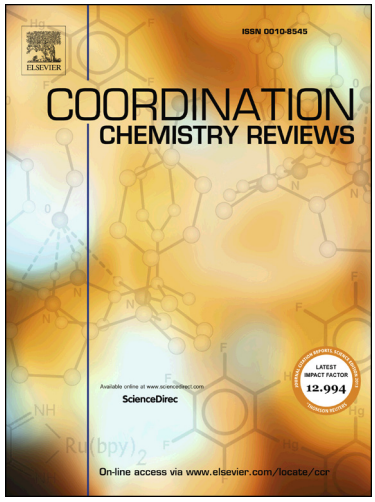

Review

Electronic structures and photophysics of d^8-d^8 complexes

Harry B. Gray, Stanislav Záliš, Antonín Vlček

PII: S0010-8545(16)30441-6
DOI: http://dx.doi.org/10.1016/j.ccr.2017.01.008
Reference: CCR 112382

To appear in: *Coordination Chemistry Reviews*

Received Date: 29 October 2016
Revised Date: 17 January 2017
Accepted Date: 18 January 2017

Please cite this article as: H.B. Gray, S. Záliš, A. Vlček, Electronic structures and photophysics of d^8-d^8 complexes, *Coordination Chemistry Reviews* (2017), doi: http://dx.doi.org/10.1016/j.ccr.2017.01.008

Electronic structures and photophysics of d^8-d^8 complexes

Harry B. Gray[a], Stanislav Záliš[b], Antonín Vlček[b,c]

[a] Beckman Institute, California Institute of Technology, Pasadena, CA 91125, United States
[b] J. Heyrovský Institute of Physical Chemistry, Czech Academy of Sciences, Dolejškova 3, 182 23 Prague, Czech Republic
[c] Queen Mary University of London, School of Biological and Chemical Sciences, Mile End Road, London E1 4NS, United Kingdom

E-mail addresses: hbgray@caltech.edu (Harry B. Gray), zalis@jh-inst.cas.cz (Stanislav Záliš), a.vlcek@qmul.ac.uk (Antonín Vlček)

Dedicated to Barry Lever, consummate scholar and treasured friend, in recognition of his deep and lasting contributions to coordination chemistry.

Abstract

Research on d^8-d^8 complexes is being actively pursued, owing, in part, to newly developed time-resolved optical, IR, and X-ray methods that directly interrogate bonding changes upon excitation. Our review covers work on the ground- and electronic excited states, as well as the oxidized and reduced forms, of these complexes. Recent experimental and theoretical results add a new chapter to the rich history of d^8-d^8 spectroscopic and chemical behavior.

Contents

1. Introduction

Many complexes of d^8 transition metals have square planar geometries. Stacking of the planar units often occurs in the solid state, producing columnar structures as in Magnus Green Salt $[Pt(NH_3)_4]^{2+}[PtCl_4]^{2-}$, known since 1828 [1]. The relatively short Pt-Pt distance of ca. 3.2 Å [2] indicates the presence of attractive Pt-Pt interactions. The 1975 report of concentration-dependent dimer and trimer formation in acetonitrile solutions of $[Rh(CNPh)_4]^+$ ushered in the modern era of d^8-d^8 spectroscopy and chemistry [3]. To describe orbital interactions, a generic d^8-d^8 MO scheme (Figure 1) was developed [3], where the $4d_{z2}$ orbitals on the two rhodium atoms interact with each other producing dσ bonding (a_{1g}) and antibonding (a_{2u}) orbitals that are both occupied. A similar combination of $5p_z$ orbitals produces empty pσ (a_{1g}) and pσ* (a_{2u}) orbitals at higher energies. $[Rh(CNPh)_4]^+$ dimerization is accompanied by emergence of a strong absorption band at 568 nm that was attributed to an allowed dσ*→pσ ($1a_{2u}\rightarrow 2a_{1g}$) transition [3]. Indeed, such a strong band in the visible or near UV region is a signature feature of electronic absorption spectra of all d^8-d^8 species. Subsequently, a great many self-assembled dimers and higher oligomers of Pd^{II}, Pt^{II}, Rh^{I}, Ir^{I}, and Au^{III} d^8 complexes with interesting structural, spectroscopic, and photoluminescence properties were characterized [4].

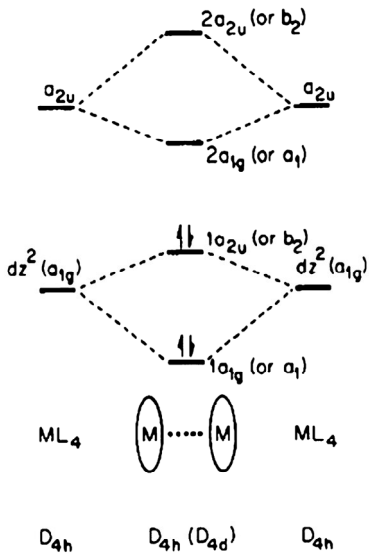

Figure 1. A generic d^8-d^8 MO scheme originally developed for $Rh_2(CNPh)_8^{2+}$ [3]. $4d_{z2}$ orbitals on the two metal centers combine in-phase and out-of-phase to produce dσ ($1a_{1g}$) bonding and dσ* ($1a_{2u}$) antibonding orbitals, respectively. Formally, no net M-M bonding arises as both orbitals are occupied. $5p_z$ orbitals combine in the same way, producing higher-lying pσ ($2a_{1g}$) and pσ* ($2a_{2u}$) orbitals, which are both empty. Reproduced with permission from ref. [3]. Copyright (1975) American Chemical Society.

As an alternative to self-assembled dimers and oligomers, the use of designed bridging ligands enabled construction of binuclear complexes with well-defined and controllable structures (Figure 2). Diisocyanide ligands "bridge" (1,3-diisocyanopropane) and TMB (2,5-dimethyl-2,5-diisocyanohexane) were used to make $Rh_2(bridge)_4^{2+}$ (Rh(bridge)) and $Rh_2TMB_4^{2+}$ (Rh(TMB)) that have relatively short metal-metal distances (3.24 Å in Rh(bridge); 3.26 Å in Rh(TMB) [5], 3.12 Å in Ir(TMB) [6]). Each of these complexes exhibits a strong dσ*→pσ visible absorption band that arises from the metal-metal interaction. Emission spectra of Rh(bridge) and Rh(TMB) measured in fluid solutions show fluorescence (656, 614 nm) and phosphorescence (865, ~780 nm) from dσ*pσ singlet and triplet states, respectively [7]. Observation of dual emission is very unusual for heavy metal complexes. The ^{1}dσ*pσ lifetime is

surprisingly long, ca. 1 ns for both Rh complexes [7]. The corresponding triplet lifetimes were determined to be 8.3 (bridge) and 0.03 μs (TMB), increasing with decreasing temperatures (12.5 and 20.5 μs at 77 K, respectively) [7]. Similar behavior was observed for diiridium complexes with bridging pyrazolyl (pz) and 3,5-dimethylpyrazolyl (pz*) ligands $Ir_2(\mu\text{-}pz)_2(COD)_2$ and $Ir_2(\mu\text{-}pz^*)_2(CO)_2(PR_3)_2$ [8-12]. Dirhodium and diiridium complexes undergo interesting photochemistry. Remarkably, visible-light irradiation of Rh(bridge) in aqueous HCl produces H_2 [13, 14] and its $^3d\sigma^*p\sigma$ state is quenched reductively as well as oxidatively with nearly diffusion-controlled rates [15]. Relatively long singlet and triplet excited state lifetimes opened the way for investigations of their properties and chemical reactivity. Indeed, it was found that both singlet and triplet $d\sigma^*p\sigma$ states of the Ir_2 unit in $Ir_2(\mu\text{-}pz^*)_2(CO)_2(Ph_2PO(CH_2)_2A^+)_2$ are oxidized by the appended pyridinium acceptor A^+ [11, 12]. These excited-state electron transfer reactions were one of the early demonstrations of the Marcus inverted region; and a theoretical treatment [16] pointed to the importance of structural fluctuations and discussed possible differences in electronic coupling to singlets and triplets.

The use of the dimen bridging ligand (1,8-diisocyanomenthane, Figure 2) [6, 17-20] led to an interesting new twist in d^8-d^8 chemistry: A long distance between the -N≡C ligating groups and one dangling $–CH_2$-N≡C moiety keep the metal atoms farther apart while introducing structural flexibility. As a consequence, the M-M distances in $M_2(dimen)_4^{2+}$ (further abbreviated M(dimen)) are highly variable and, in the solid state, depend on the counter anion. X-ray values range from 3.6 to 4.4 Å for Ir and 3.9 – 4.5 Å for Rh [6, 21], attesting to a shallow potential energy minimum along the M-M coordinate. Importantly, the dimen ligand dimensions alone require the two metal atoms to be ca. 5 Å apart; shorter bond distances are achieved only at

the expense of ligand distortions [21]. The long metal-metal distance and fluctional ground-state geometry strongly broaden and shift the $d\sigma^*p\sigma$ absorption band [19, 21] of dimen complexes, while preserving well-defined and long-lived fluorescence (230 ps at 295 K for Rh) and phosphorescence (21 μs at 77 K) [19].

The electrochemistry of dirhodium isocyanide complexes has received relatively little attention. Oxidation is irreversible, coupled with dimerization or ligand coordination (solvent, halide) in the axial positions [18, 22]. Reversible reduction reported [23] for Ir(dimen) occurs in two subsequent 1-electron steps whose products were characterized by IR spectroelectrochemistry. The first reduction produces a symmetrical $Ir(dimen)^+$ species with a $(d\sigma^*)^2(p\sigma)^1$ electronic configuration. The second step leads to an asymmetric $Ir(dimen)^0$ complex for which a mixed-valence Ir^{I}-Ir^{-I} d^8-d^{10} configuration was proposed [23].

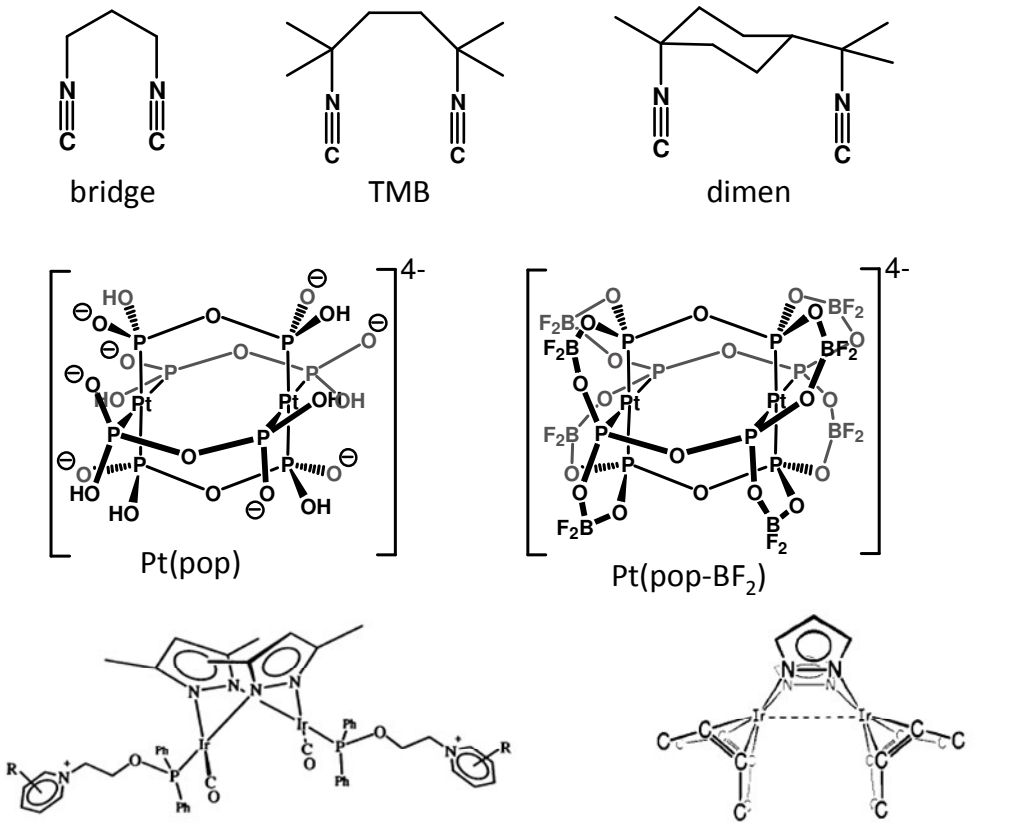

Figure 2. Schematic structures of the bridging ligands and selected d^8-d^8 complexes discussed in this review. "Historic" ligand abbreviations consistent with original papers are used. Simplified abbreviations of the type M(bridging ligand) are used throughout this paper.

A very important entry in d^8-d^8 chemistry, spectroscopy, and photophysics was the binuclear Pt(II) μ-diphosphito complex $[Pt_2(P_2O_5H_2)_4]^{4-}$, abbreviated Pt(pop) (Figure 2) [24-29]. In 1977, intense green emission from a product of a reaction between K_2PtCl_4 and phosphorous acid was reported [30]. (It is likely that this compound was made first in 1957 [31, 32]. The structure of the emissive species was determined in 1980 [33, 34].) Detailed spectroscopic studies followed immediately [35-44]. Each Pt atom occurs in square-planar coordination with four P atoms; and the two PtP_4 planes are held parallel by four P-O-P links at a Pt-Pt distance of 2.93 Å (Bu_4N^+ salt, [45]). The complex exhibits strong (37500 $M^{-1}cm^{-1}$) $d\sigma^* \rightarrow p\sigma$ near-UV

absorption at 372 nm, weak short-lived fluorescence (0.7-30 ps, depending on solvent [46-48]), and long-lived (9.4 μs [42, 49]) strong phosphorescence in fluid solution. Several weak UV absorption bands were attributed to LMMCT (ligand to metal-metal CT) transitions of strongly mixed singlet-triplet character [50]. Pt(pop) undergoes interesting photoreactivity from the $^3d\sigma^*p\sigma$ excited state, including: H-atom abstraction from main-group metal hydrides whose kinetics point to radical-like behavior [51-53]; catalytic dehydrogenation of secondary alcohols [26, 28, 53]; and inner-sphere electron transfer with $[Co(CN)_5X]^{3-}$ complexes accompanied by transfer of the halide ligand X [54, 55]. The $^3d\sigma^*p\sigma$ state is quenched by energy transfer as well as by oxidative (e.g. methylviologen) and reductive (aromatic amines) electron transfer, with nearly diffusion-controlled rates (depending on driving force) and ≥80% cage-escape yields [49, 56]. An interesting perfluoroborated derivative of Pt(pop) containing no hydrogen atoms, in which the pop ligands are covalently linked by BF_2 groups, was prepared recently: $[Pt_2(P_2O_5(BF_2)_2)_4]^{4-}$, abbreviated Pt(pop-$BF_2$) [57]. This complex preserves all the structural and spectroscopic features of Pt(pop) while the ligand cage is much more rigid and the $Pt_2(POP)_4$ core is better shielded from the environment by BF_2 groups, with eight F atoms on the outer surface (Figure 2). Absorption spectral features are shifted to higher energies relative to Pt(pop): the $^1d\sigma\rightarrow{}^*p\sigma$ absorption peaks at 365 nm; and the UV LMMCT bands undergo larger shifts [57]. Of interest is that the fluorescence following excitation of Pt(pop-BF_2) is much stronger and more than 2000-times longer-lived (1.6 ns at room temperature) than in Pt(pop). With the overall emission quantum yield approaching unity, the complex behaves as a dual emitter [57, 58] that has potential application as a luminescence oxygen sensor [59].

Like dirhodium(I) and diiridium(I) isocyanide complexes, electrochemical oxidation of Pt(pop) and Pt(pop-BF_2) is an irreversible 2-electron process coupled with axial ligand coordination [60, 61]. Although electrochemical reduction of Pt(pop) has not been reported, electrochemiluminesce was observed in MeCN upon fast potential switching [62, 63]. In contrast, Pt(pop-BF_2) undergoes two successive 1-electron reductions producing Pt(pop-BF_2)$^{5-}$ $(d\sigma^*)^2(p\sigma)^1$ and superreduced Pt(pop-BF_2)$^{6-}$ with a unique $(6p\sigma)^2$ bond [61].

A different class of d^8-d^8 diplatinum compounds includes [Pt(ppy)(μ-^{t}Bu$_2$pz)]$_2$ (ppy = 2-phenylpyridine, ^{t}Bu$_2$pz = 3,5-di-*tert*-butylpyrazolate) and its derivatives. Introducing the electron-accepting ppy ligand changes the nature of the lowest excited state to $d\sigma^* \rightarrow \pi^*$(ppy) MMLCT (metal-metal to ligand charge transfer). The corresponding triplet exhibits interesting photophysics [64-69].

Research on binuclear d^8-d^8 complexes is booming, fueled by the quest for new molecular photonic materials as well as the desire for fundamental understanding of metal-metal bonding and excited-state dynamics. Synthesis and characterization of new types of d^8-based self-assembled oligomers has produced strongly luminescent materials with interesting applications in molecular recognition, as OLED dopants, sensors, and bioimaging agents, as well as in molecular electronics. As the chemistry of self-assembled d^8 systems has recently been reviewed in great depth [4], we will focus attention on bridged d^8-d^8 complexes, namely Pt(pop) /Pt(pop-BF_2) and Ir(dimen), where current work involving state-of-the-art laser spectroscopic techniques and quantum chemical calculations has shed new light on metal-metal bonding and excited-state dynamics. Qualitative MO considerations (Figures 1, 3) suggest that metal-metal interactions will be strengthened upon electronic excitation and reduction that populate the pσ

bonding orbital. Describing such redox- and excitation-induced bonding changes is particularly challenging for theory; and, on the experimental side, new ultrafast time-resolved spectroscopic techniques in the UV-visible [47, 48, 70] and X-ray [71-73] spectral ranges can be employed to examine structural effects of electronic excitation as well as to reveal molecular dynamics on corresponding potential energy surfaces. Combining spectroscopic studies with DFT calculations [21, 61] provided still deeper insights, especially when spin-orbit coupling [50] and molecular dynamics [48, 74-76] were included. Electrochemical and spectroelectrochemical techniques together with DFT calculations revealed new types of metal-metal bonding in the reduced states of d^8-d^8 complexes [23, 61]. The emerging understanding of excited-state and redox behavior of d^8-d^8 systems opened the way for exploration of photo- and electrocatalysis as well as molecular photonics. The Pt(pop) / Pt(pop-BF_2) and Ir(dimen) systems that will be discussed in detail represent structural extremes: The Pt complexes are compact and rigid, with short metal-metal distances, whereas Ir(dimen) features an exceptionally long Ir-Ir bond that can be manipulated by interactions with the medium.

2. Electronic ground states: bonding and spectra

The generic MO scheme (Figure 1) originally developed [3] for self-assembled $[Rh_2(CNPh)_4]^{2+}$ is a good starting point to discuss metal-metal interactions in d^8-d^8 complexes. Formation of the $d\sigma^*$ HOMO and $p\sigma$ LUMO accounts for the strong $^1d\sigma^* \rightarrow p\sigma$ absorption signature of d^8-d^8 systems. However, there is no net bonding, since both the HOMO and LUMO are fully occupied. Accordingly, a theoretical analysis of $Rh_2(CNPh)_8^{2+}$ gave only a very small (0.018) Rh-Rh Wiberg bond order [77]. Notably, the work emphasized that London dispersion

forces between the phenyl rings more than compensate for the repulsive interactions between positively charged $Rh(CNPh)_4^+$ fragments [77]. In this analysis, only 10-15 % of the attractive forces resulted from metal-metal (d^8-d^8) interactions attributed to "medium-range" electron correlation effects [77].

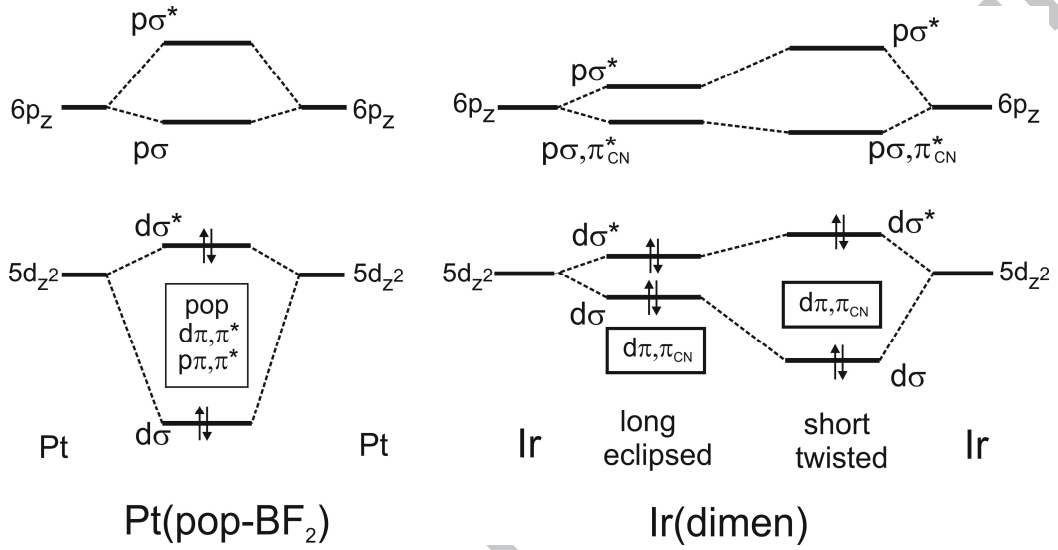

Figure 3. Qualitative MO schemes of Pt(pop-BF_2) and Ir(dimen). In the Pt complex, the dσ* and dσ orbitals are the HOMO and HOMO-16, respectively. They are separated by a large energy gap, in which there is a manifold of occupied pop-localized orbitals, usually mixed with Pt-Pt dπ, dπ* and pπ, pπ*. The long/eclipsed M(dimen) isomer exhibits a relatively small dσ* – dσ splitting. In the short/twisted isomer, this splitting increases and the dσ*, dσ orbitals are separated by a manifold of Ir-Ir dπ, dπ* orbitals with a 20-30% π(CN) admixture. MO shapes are shown in Figure 4.

Structures of Rh(bridge), Rh(TMB), Pt(pop), Pt(pop-BF_2), and M(dimen) (M = Rh, Ir) are dictated by the geometries of the bridging ligands, or more precisely, by the balance between the weak M-M attractive interactions and the strain imposed on the bridge. This strain likely is small in the ligand cages of Pt(pop) and Pt(pop-BF_2) that fix the Pt atoms 2.93 (solid Bu_4N^+ salt as well as EtOH solution [45, 71, 78, 79]) and 2.887 Å (solid Ph_4As^+ salt [57]) apart, respectively, essentially preserving planar coordination around each Pt center. (We say "ligand cages" since

the bridging ligands are stitched together by H-bonds or BF_2 groups.) Eclipsed and staggered conformers of Pt(pop) were identified by DFT calculations [50, 80]. They differ mainly by the relative orientations of O···H–O' motifs. (The two PtP_4 units are nearly eclipsed (P-Pt-Pt-P dihedral angle of 7.2^o) even in the O···H–O' staggered conformation.) The eclipsed conformation was calculated to be more stable by 0.012 eV (in vacuum). On the other hand, Pt(pop-BF_2) occurs only in the eclipsed conformation. The Mayer-Millikan bond order of 0.173 calculated for Pt(pop-BF_2) indicates a weak Pt-Pt covalent interaction [61]. (See [81] for bond-order definitions.)

The situation is more complicated for M(dimen). Whereas unperturbed dimen would hold the metal atoms ~5.2 Å apart [6, 21], experimentally determined Ir–Ir bond lengths are shorter, varying between 3.6 and 4.4 Å, depending on the counter anion [6, 21]. To account for the structural and spectroscopic data, it was proposed [6] and later supported by DFT analyses [21, 70, 82] that there are two Ir(dimen) deformational isomers, long/eclipsed and short/twisted. Their presence in MeCN solution was confirmed by X-ray scattering that determined Ir–Ir distances of 4.3(1) and 3.60(9) Å, respectively [72]. A twist angle between the IrC_4 planes of 14.6-38.4° was calculated by DFT for the latter [70, 82]). A detailed DFT structural analysis of dimen [21] attributed the structures of the two isomers to a balance between metal-metal bonding, ligand deformation, and twisting in the horizontal symmetry plane required to accommodate the short M-M bond. Two minima on the ground-state potential energy surface of Ir(dimen) corresponding to the two deformational isomers were predicted: ~4.1 Å, 0° and ~3.6 Å / 12° – very close to experimental values. Importantly, it was shown experimentally [21] that the two isomers are in thermal equilibrium in solution (2:1 MTHF/EtCN) that shifts toward

the short/twisted isomer as the temperature decreases. On the other hand, a single Rh(dimen) long/eclipsed isomer (Rh–Rh: 4.6 Å) featuring a highly anharmonic potential energy surface was predicted by DFT calculations of the whole molecule [83] as well as by a DFT dimen-ligand analysis [21], in agreement with the lack of temperature dependence of UV-vis absorption spectra [19]. Apparently, the weaker Rh-Rh interaction (relative to Ir–Ir) is not sufficient to overcome the dimen ligand strain required to populate a short/twisted isomer in solution [21]. On the other hand, two isomers were identified in the solid state, depending on the counter anion: PF_6^- (4.48 Å, 0°) and BPh_4^- (3.86 Å, 16.2°) [19].

The metal-metal stretching vibration (ν(M-M), a_{1g} symmetry) is Raman-active; its frequency reflects the strength of M-M bonding together with the resilience of the bridging ligands. The Pt-Pt vibration in Pt(pop) occurs at 118 (H_2O solution) and 110 cm^{-1} (solid Ba^{2+} and Bu_4N^+ salts) [37, 84]; it is 123 cm^{-1} for solid $(Bu_4N)_4[Pt(pop\text{-}BF_2)]$ [58]. Very similar experimental values were obtained from resonance [37] and non-resonance Raman spectra [58], from vibronic structures of phosphorescence and fluorescence bands [35, 36, 43, 58], and from impulsive stimulated Raman scattering observed after femtosecond $d\sigma^* \rightarrow p\sigma$ excitation [47, 48, 85]. Experimental values are in excellent agreement with DFT calculations [58, 80]. Lower values were reported for Rh(bridge) (79 cm^{-1} in MeCN [86]), Rh(TMB) (55 cm^{-1}, [19]) and Rh(dimen) (28 cm^{-1} in MeCN, [19]). The long/eclipsed and short/twisted Ir(dimen) isomers are clearly distinguished by very different ν(Ir-Ir) values: 11 and 48 cm^{-1}, respectively, determined by impulsive stimulated Raman scattering using two different excitation wavelengths that selectively excite the two isomers [70].

Although metal-metal orbital interactions shown in Figures 1 and 3 lead only to weak M-M bonding, they determine the chemistry, photochemistry, spectroscopy, and photophysics of d^8-d^8 complexes. Several properties of the molecular orbitals are worth mentioning in this respect: (i) The dσ* HOMO is axially directed outwards (Figure 4) with an electron density available for interactions with Lewis acidic cations (Ag^+, Tl^+, Au^+) [87, 88] as well as for oxidative addition of halogens or alkyl halides [25, 27], which is more favorable for Pt(pop) than for Pt(pop-BF_2) [89]. (ii) The pσ LUMO is partly localized between the Pt atoms (~43 % $6p_z$) [50] and partly delocalized over the planar faces of the molecule (Figure 4), owing to the involvement of $3p_z$ orbitals of the four phosphorus atoms. The Ir(dimen) LUMO is delocalized in a somewhat different way [82]. In both isomers, it is 34-36% Ir $6p_z$ that overlaps with the π_z*(C≡N) orbitals that are oriented along the z axis and contribute ca. 60%. The pσ LUMO thus acquires π-bonding and π-antibonding character with respect to Ir–C and C≡N bonds, respectively, whereas outward localization is less pronounced than in Pt(pop)/Pt(pop-BF_2) (Figure 4); (iii) A manifold of occupied ligand-localized orbitals, some with dπ and pπ Pt-Pt admixtures, falls between the dσ* HOMO and dσ HOMO-16 in Pt(pop) and Pt(pop-BF_2) [50]. A similar manifold of mixed dπ-π(C≡N) MOs lies between dσ and dσ* orbitals in the short/twisted Ir(dimen) isomer and below dσ in the long/eclipsed one [82]. Electronic excitation from these orbitals to the LUMO gives rise to higher-lying excited states and UV absorption bands; (iv) The LUMO is separated from LUMO+1 (Pt(dδ)/σ*(PtP)) by large energy gaps (16530 and 18710 cm^{-1} for Pt(pop) and Pt(pop-BF_2), respectively). For Ir(dimen), the gap between LUMO and LUMO+1 (pσ*/π*(C≡N)) depends on the isomer: 14520 (short/twisted) and 6130 cm^{-1} (long/eclipsed), reflecting the strength of the metal-metal interaction.

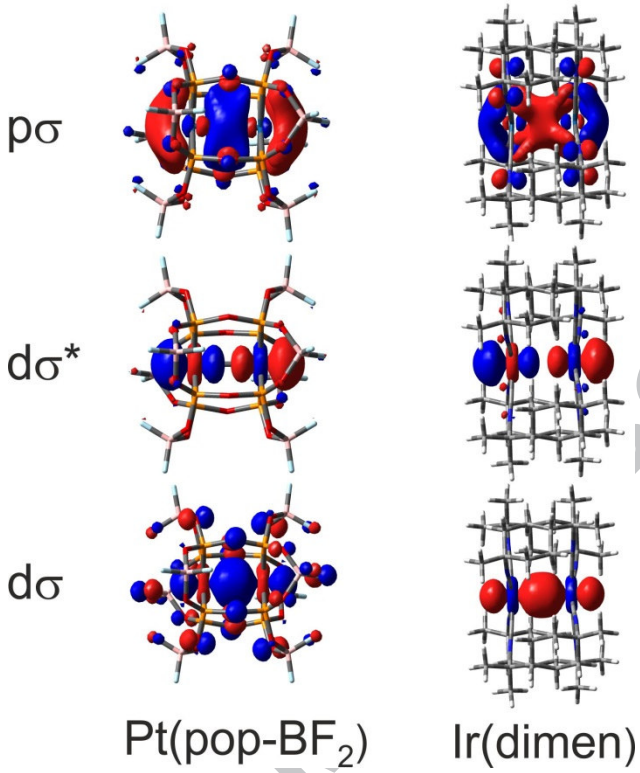

Figure 4. DFT-calculated molecular orbitals involved in metal-metal σ-bonding in Pt(pop-BF_2) and the short/twisted isomer of Ir(dimen). (DFT: GD3, PBE0/PCM-MeCN; this work). Similar MO shapes were reported for Pt(pop) [50, 87, 90, 91] and Rh(bridge) [92].

The lowest absorption bands in the UV-vis absorption spectra of d^8-d^8 complexes are attributable to dσ*→pσ transitions. For Pt(pop) and Pt(pop-BF_2), the triplet and singlet dσ*→pσ transitions were observed as weak and strong bands, respectively, both with symmetrical shapes (Figure 5) [24, 35, 36, 42, 57]. Assignments of these absorptions, which have no counterpart in the spectra of monomeric Pt^{II} complexes, were confirmed by analysis of single-crystal polarized spectra [36, 42], MCD spectra [93], as well as by spin-orbit DFT calculations [50]. The ^{1}dσ*→pσ peak energy is nearly solvent-independent (varying within a ~300 cm^{-1} range in MeCN, DMF, H_2O, EtOH, ethylene glycol [46, 48]; and the ^{1}dσ*→pσ band

shifts by only ~400 cm^{-1} to higher energy on going from Pt(pop) to Pt(pop-BF_2), although the $^3d\sigma^* \rightarrow p\sigma$ energy is constant. Diiridium(I) and dirhodium(I) isocyanide complexes exhibit $^1d\sigma^* \rightarrow p\sigma$ transitions at lower energies, with asymmetric bands in the visible spectral region. Ir(dimen) is a particularly interesting case, as it has two bands (470 and 580 nm) in solution (Figure 6) attributed to long/eclipsed and short/twisted isomers, respectively [21] (the intensity ratio changes with temperature due to the equilibrium between the two isomers). On the other hand, the $^1d\sigma^* \rightarrow p\sigma$ band shape and peak position of Rh(dimen) are very similar in room-temperature MeCN solution and in MeTHF/MeCN glass at 77 K [19], indicating that a single species is present. The Rh(dimen) spectrum has a sharp peak at 423 nm with a low-energy shoulder at ~480 nm that tails beyond 500 nm. As the intensity of the shoulder is too high for a triplet transition, the unusual band shape was explained by a combination of a very shallow ground-state potential energy surface with an anharmonic excited-state surface whose minimum occurs at a shorter Rh-Rh distance. In this model, absorbance around the peak maximum would correspond to excitation to higher vibrational levels of the $^1d\sigma^*p\sigma$ state, whereas the shoulder would arise from vibronic transitions closer to the excited-state energy minimum [19]. (Newer calculations [21, 83] found both ground- and excited-state highly anharmonic with very different shapes, which is in agreement with the above qualitative explanation.) The spin-forbidden $^3d\sigma^* \rightarrow p\sigma$ transition likely is obscured by the red shoulder; it was identified only in the polarized single-crystal spectrum of [Rh(dimen)](BPh_4)$_2$, occurring about 3000 cm^{-1} below the singlet absorption [19]. Complexes with shorter bridging ligands, Rh(bridge), Rh(TMB), and Ir(TMB), exhibit $^1d\sigma^* \rightarrow p\sigma$ absorption bands at 553, 517, and 625 nm, respectively [13, 94]. Symmetrical band shapes suggest harmonic ground- and excited-state

potentials whose minima are shifted with respect to each other. Molar absorptivities are in the 11000-14500 $M^{-1}cm^{-1}$ range, 30-50% of the Pt(pop) values.

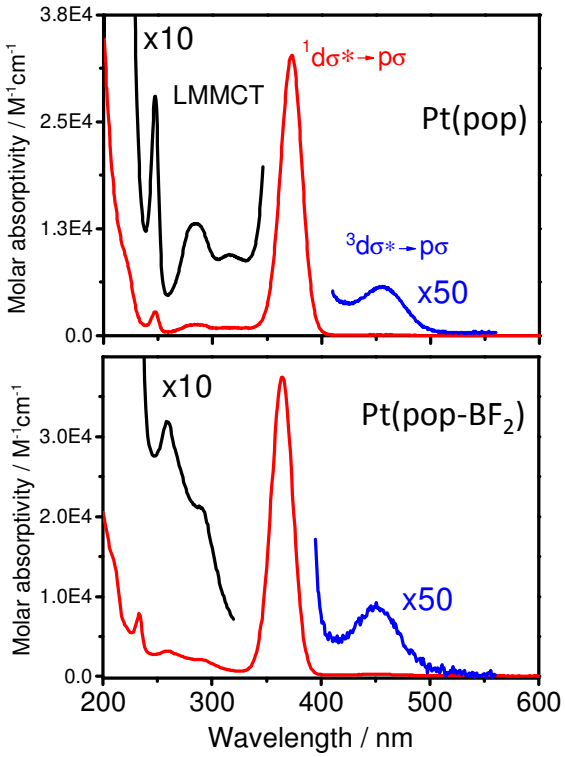

Figure 5. UV-vis spectra of Pt(pop) and Pt(pop-BF_2) in MeCN.

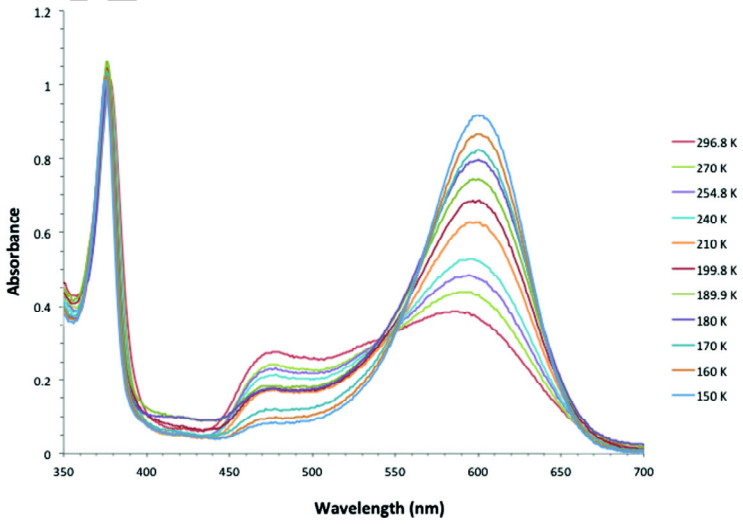

Figure 6. Temperature dependence of UV-vis spectra of Ir(dimen) in 2:1 2-MeTHF/EtCN. Reproduced with permission from ref. [21]. Copyright (2012) American Chemical Society.

The nature of higher electronic transitions in the UV is different for Pt^{II} and Ir^{I}/Rh^{I} isocyanide complexes. Pt(pop) shows three relatively weak UV peaks that shift to higher energies by up to 1300 cm^{-1} as the solvent changes from MeCN and DMF to H_2O, EtOH and ethylene glycol [42, 46, 48]. Pt(pop-BF_2) exhibits the same UV spectral pattern, the three bands occurring on average at energies 2750 cm^{-1} higher than in the Pt(pop) spectrum (Figure 5) [57]. As the corresponding transitions have mixed-spin character, assigning the UV bands requires taking into account spin-orbit (SO) coupling [50]. SO-TDDFT calculations revealed a dense manifold of triplet and mixed-spin states with zero and moderate oscillator strengths, respectively, with origins 4200 (Pt(pop)) and 5800 cm^{-1} (Pt(pop-BF_2)) above the $^1d\sigma^*p\sigma$ state. These states involve LMMCT excitations from pop-localized orbitals to the $p\sigma$ LUMO; and some of them have small (~10 %) $p\pi\rightarrow p\sigma$ and, at higher energies, larger $d\pi\rightarrow p\sigma$ contributions [50]. (The $p\pi$ contributions arise from small Pt $6p_{x,y}$ admixtures to predominantly pop-localized orbitals.) The first and second UV absorption systems of both Pt(pop) and Pt(pop-BF_2) are due to several LMMCT/$p\pi\rightarrow p\sigma$ E_u transitions with 2-13% singlet and ~86% singlet character, respectively. (In addition, a ~2% singlet A_{2u} transition contributes to the second UV band as well.) The highest UV band originates from several closely spaced (two LMMCT/$d\pi\rightarrow p\sigma$ and one LMMCT) transitions (60-80% singlets).

The UV spectrum of Ir(TMB) in MeCN exhibits sharp, intense bands at 372 and 318 nm (340 and 314 nm for Rh(TMB)) assigned to triplet and singlet $d\pi\rightarrow p\sigma$ E_u transitions, respectively, based on single-crystal polarized spectra and MCD spectra [94]. The lower spin-forbidden transition gains intensity through SOC that is rather strong among $d\pi p\sigma$ states [50].

This assignment is supported by the relative intensities, whereby the molar absorptivity of the $^3d\pi\rightarrow p\sigma$ 372 nm band (9750 $M^{-1}cm^{-1}$) is ~2.3× weaker than the spin-allowed $^1d\pi\rightarrow p\sigma$ 318 nm band. Also, it is 2.3× stronger than the $^3d\pi\rightarrow p\sigma$ 340 nm band of Rh(dimen), since Rh has lower SOC than Ir. Owing to large d_{xz},d_{yz} participation in the dπ molecular orbital (~70%) and π*(C≡N) participation in the pσ LUMO, the two UV transitions of Ir(TMB) (and other Rh and Ir di-isocyanides) should be described as predominantly (M)MLCT. Experimentally, the delocalization over the C≡N– groups is manifested by a ν(C≡N) vibronic satellite on the $^3d\pi\rightarrow p\sigma$ Ir(TMB) band [94]. Broad weaker bands observed in the Ir(TMB) spectrum around and below 300 nm were tentatively attributed to singlet and triplet $d\delta\rightarrow p\sigma$ and singlet MMCT transitions. The latter would produce zwitterionic states $M^{II}M^0$, predicted by valence-bond analysis by exciting a $d_{xz,yz}$ electron from one metal atom to the p_z orbital at the other [94]. UV spectra of Rh(dimen) [19] and Ir(dimen) [23] are very similar to those of their TMB counterparts. In particular, the UV spectrum of Ir(dimen) [23] exhibits triplet and singlet $d\pi\rightarrow p\sigma$ bands at 375 (ε = 18000 $M^{-1}cm^{-1}$) and 327 (36600 $M^{-1}cm^{-1}$) nm, respectively.

Computational studies of d^8d^8 systems have focused on Pt(pop) in the ground and $^3d\sigma^*p\sigma$ states. Initial calculations on Pt(pop) in vacuum well reproduced the crystallographic structural parameters [80, 90], revealed the occurrence of energetically close staggered and eclipsed conformations (see above), assigned Raman and IR active vibrations [80], partitioned contributions to the Pt-P and Pt-Pt interactions, and predicted bonding changes upon excitation [90]. Gas-phase excitation energies and calculated bond-length changes were found to be strongly dependent on the functional. Energies of the HOMO and other occupied MOs were calculated to be highly positive, apparently due to the lack of electrostatic screening of the 4–

charge of the complex. A following study [91] clearly demonstrated the importance of including solvent (H_2O, continuum dielectric model CPCM) into DFT (B3LYP) calculations. Negative energies of occupied orbitals, a reasonable HOMO-LUMO energy gap, and the correct $^1d\sigma^* \rightarrow p\sigma$ assignment of the lowest allowed transition were obtained only in PCM-described H_2O [91]. (PCM-H_2O calculations correctly produced a $p\sigma$-type LUMO, partly delocalized over the P,O ligand atoms. In contrast, a predominantly Pt 6s antibonding LUMO was calculated in the gas phase [91].) This study [91] also predicted that the lowest UV transition would have LMMCT character. Solvent effects on the ground-state structure also were investigated by quantum mechanics/molecular mechanics (QM/MM) simulations in H_2O, DMF, and EtOH, with the aim of demonstrating how solvation influences EXAFS spectra [79]. QM/MM average Pt-Pt distances were slightly longer (3.06 – 3.08 Å) than when the solvent was treated by continuum models (~3.04 Å in H_2O [91]; 2.924 Å in MeCN [50]) whereas Pt-P lengths (2.41-2.42 Å) were calculated comparable in H_2O (~2.40 Å [91]) and longer than in MeCN (2.332 Å [50]). (For comparison, Pt–Pt distances of 2.88-2.93 (EtOH) and 2.98 Å (H_2O) were determined experimentally in solution by EXAFS [71, 78, 79] and X-ray scattering [95], respectively.) Electronic structures of Pt(pop) and Pt(pop-BF_2) were compared using SO-TDDFT calculations that also accounted for spin-forbidden $^3d\sigma^* \rightarrow p\sigma$ transitions and assigned UV absorption bands, revealing their mixed-spin character [50] (see above). These calculations reproduced the experimentally observed shortening of Pt-Pt and Pt-P bonds and blue shifts of electronic transitions upon perfluoroboration. Electronic structures of the two complexes are qualitatively very similar (stronger Pt-Pt and Pt-P bonds together with increased rigidity were demonstrated by ν(Pt-Pt) and ν(Pt-P) stretching frequencies that increased from ~116 and 232

cm^{-1}, respectively, in Pt(pop) [37, 80] to 123 and 283 cm^{-1} in Pt(pop-BF_2) [58]; the experimental and calculated values matched very well). Less attention has been devoted to computational investigations of bridged Ir^{I} and Rh^{I} complexes. DFT-calculated (gas-phase) Rh(bridge) and Rh(dimen) HOMO and LUMO shapes are shown in [92] and [83], respectively. Dimen-ligand [21] and Ir(dimen) whole-molecule [70, 82] calculations addressed the structures and relative stabilities of the two isomers, as discussed above.

The relative importance of covalency and dispersion to the ground-state metal-metal interaction is another interesting question. As was discussed above, dispersion is the main attractive force in unbridged assemblies such as $Rh_2(CNPh)_8^{2+}$ [77], where it is aided by the nearly parallel large π-delocalized ligand systems at each metal center. Structural and bonding effects of including the dispersion correction in the DFT calculations are given in Tables 1 and 2. Dispersion strengthens the Ir-Ir interaction in Ir(dimen), presumably due to the presence of C≡N– π electrons. Including dispersion into the calculation through a GD3 correction [96] shortens the Ir–Ir distance in the long/eclipsed isomer by 0.4 Å (Table 1) and increases the Mayer-Mulliken bond order from 0.044 to 0.072. The GD3-calculated Ir–Ir distance is very close to the experimental value of 4.3 Å measured in MeCN solution [70]. The GD3 correction enabled optimization of the short/twisted isomer that did not converge when dispersion was not included. The calculated Ir-Ir distance is in a reasonable agreement with the experimental value of 3.60 Å. On the other hand, dispersion forces are relatively unimportant in Pt(pop-BF_2) where the metal-ligand planes are formed by more electronegative phosphorus atoms with relatively localized electron density and no π-electrons. Accordingly, GD3 had only negligible effect on the Pt–Pt distance that was calculated (Table 1) close to the experimental (solid state)

value of 2.887 Å [50]. Of interest is that the Pt-P distances contract slightly upon correcting for dispersion (from 2.308 to 2.295 Å). The Pt–Pt and Pt–P bond orders are little affected by the GD3 correction, regardless of Pt(pop-BF_2) redox- and electronic state (Table 2). The only real difference was found for the parent complex, where the Pt-Pt bond order increases by 35% upon GD3 correction. This finding could be related to the involvement of bridging O atoms in the dσ orbital (Figure 4) that would be larger in a "flatter" GD3-corrected structure.

Table 1. Metal–metal distances in Ir(dimen)^n and Pt(pop-BF_2)^n in various redox and electronic states calculated by solvent-corrected DFT without and with the GD3 correction of dispersion forces [this work]. Not converging optimization is denoted x.

Ir(dimen) / n	**2+**		**1+**	**0**		**2+ / ^{3}dσ*pσ**
	long	short	[a]	eclipsed	twisted	[a]
no dispersion	4.752	x	3.936	3.709	3.124	2.910
GD3 correction	4.319	3.251	3.087	3.088	2.988	2.857
Pt(pop-BF_2) / n	**4-**		**5-**	**6-**		**4- / ^{3}dσ*pσ**
no dispersion	2.904		2.803	2.739		2.708 [b]
GD3 correction	2.901		2.815	2.740		2.715

[a] A single stable structure was found by DFT. [b] A value of 2.725 Å was reported in [50]. The difference is caused by a different basis set used in the present calculation. See the Appendix for details.

Table 2. DFT-calculated (GD3, PBE0/PCM-MeCN) Mayer-Mulliken bond orders for Pt(pop-BF_2)^n [this work]. Values calculated without the GD3 dispersion correction in parenthesis. Pt–P values are averaged over the two Pt centers.

bond / n	**4-**	**5-**	**6-**	**4- / ^{3}dσ*pσ**
Pt – Pt	0.233 (0.173)	0.268 (0.268)	0.341 (0.340)	0.521 (0.523)
Pt – P1	1.118 (1.119)	1.181 (1.181)	1.178 (1.175)	1.083 (1.082)
Pt – P2	1.118 (1.119)	1.173 (1.173)	1.309 (1.309)	1.086 (1.086)
Pt – P3	1.118 (1.122)	1.173 (1.173)	1.701 (1.167)	1.083 (1.082)
Pt – P4	1.118 (1.119)	1.181 (1.182)	1.309 (1.312)	1.086 (1.086)

3. Excited states: structures and bonding

Interactions between d^8 metal centers give rise to unique excited-state structures and behavior, including: M-M bond formation upon excitation, long lifetimes (ps-ns) of the lowest singlet excited state [7, 8, 11, 19, 46-48, 57, 58, 70, 97], dual emission [7, 19, 57, 58], μs-lived phosphorescence, and rich photochemistry including electron and energy transfer, as well as radical-like atom-transfer reactions [8, 11, 13-15, 24-28, 49, 51-55, 89, 98]. Although d^8-d^8 excited states have been studied by powerful experimental and theoretical techniques, photophysical properties are still not sufficiently understood, as for example the mechanism of (symmetry forbidden) intersystem crossing and its dependence on structure, solvent, and temperature. Other areas of great current interest include coherent motions induced by femtosecond excitation, comparing the structures and reactivities of singlet and triplet excited states, relaxation pathways of higher excited states, as well as possible applications in photocatalysis.

In agreement with qualitative MO theory (Figures 1, 3), SO-TDDFT calculations of Pt(pop) and Pt(pop-BF_2) confirmed [50] that the lowest singlet ($^1A_{2u}$) and triplet ($^3A_{2u}$) excited states arise almost exclusively (95 %) from $d\sigma^* \rightarrow p\sigma$ (HOMO→LUMO) excitation. The $^1A_{2u}$ state has additional (albeit small) contributions from high-lying LMMCT/$p\pi p\sigma$ and LMMCT/$d\pi p\sigma$ triplet states, admixed through spin-orbit coupling. The $^3A_{2u}$ state splits into three SO components (A_u, aB_u, bB_u) in the correct (C_{2h}) symmetry. However, the aB_u-bB_u splitting is too small to be distinguished experimentally and low-temperature high-resolution spectra therefore were interpreted in terms of A_{1u} + E_u SO states, assuming D_{4h} Pt_2P_8 core symmetry. The A_{1u} state is a pure triplet: 98% $^3d\sigma^*p\sigma$, with minor contributions from higher triplets; and

E_u is 98% $^3d\sigma^*p\sigma$, with minor contributions from higher triplets (~1.3%) and LMMCT/$d\pi p\sigma$ singlets (0.6-0.7%) [50].

The predominant $d\sigma^* \rightarrow p\sigma$ origin of the lowest excited singlet as well as triplet states suggests that there is substantial strengthening of the metal-metal bond upon excitation. It is worth noting that metal-metal bond strengthening in $d\sigma^*p\sigma$ excited states was first predicted and documented in the early days of d^8-d^8 spectroscopy when experiments confirmed changes of ν(M-M) stretching frequencies and bond lengths calculated from Franck-Condon (FC) analyses of absorption and emission bands [35-37, 41-43]. In the case of Pt(pop), the $^3A_{2u}$ ν(Pt-Pt) frequency of ~155 cm^{-1} was extracted from a vibrational progression of the spin-forbidden $^3A_{2u}$ absorption band of the Ba^{2+} salt; and the Pt-Pt bond distance was calculated to be 2.71 Å [36]. Comparison with respective ground-state values of ~110 cm^{-1} (determined from the phosphorescence vibrational progression and non-resonant Raman spectrum [36, 84]) and 2.949 Å [44] supports the expected strengthening of Pt–Pt bonding. Measuring vibrational progressions of both the spin-allowed and spin-forbidden $d\sigma^*p\sigma$ absorption bands of solid $(Bu_4N)_4$[Pt(pop)] yielded ν(Pt–Pt) values for the $^1d\sigma^*p\sigma$ (145-147 cm^{-1}) and $^3d\sigma^*p\sigma$ (~150 cm^{-1}) states, indicating slightly stronger bonding in the excited triplet. (The ground-state ν(Pt-Pt) frequency was 116 cm^{-1} [84].) A stronger Pt-Pt interaction in $^3d\sigma^*p\sigma$ than $^1d\sigma^*p\sigma$ also was indicated for $(Bu_4N)_4$[Pt(pop-BF_2)], where values of 168 and 160 cm^{-1}, respectively, were determined from vibronic structures in the corresponding excitation spectra [58] as well as by impulsive Raman scattering upon femtosecond excitation [85]. (Ground state: 123 cm^{-1} [58]) Ground- and $^3d\sigma^*p\sigma$ excited-state ν(Pt–Pt) values of Pt(pop) also were obtained in aqueous solution using transient Raman spectroscopy: 118 and 156 cm^{-1}, respectively [37]. Similar

behavior was reported for Rh(bridge): the ground-state Raman ν(Rh–Rh) band at 79 cm^{-1} (in MeCN) shifted upon nanosecond laser-pulsed excitation to 144 cm^{-1} [99], in agreement with the ~150 cm^{-1} vibrational progression of the lowest absorption band corresponding to the spin-forbidden $^3(d\sigma^* \rightarrow p\sigma)$ transition [86]. FC analysis of the absorption system yielded a 0.3 Å Rh-Rh contraction upon excitation, from 3.24 to 2.94 Å [86].

The change of the M-M force constant upon excitation reflects the bond strengthening/shortening that is, however, limited by the bridging ligand geometry and flexibility. The Pt-Pt force constant in Pt(pop) increases 1.8-times upon excitation while the Rh-Rh force constant in Rh(bridge) increases 3.3-times [37]. In absolute values, however, both ground- and excited-state Pt-Pt force constants (0.80, 1.40 mdyn $Å^{-1}$) are larger than the Rh ones (0.19, 0.63 mdyn $Å^{-1}$). It appears that the pop ligand cage restricts changes in the M-M distance more than "bridge", while keeping the two Pt atoms closer together both in the ground and excited states [37]. The effect of the bridging ligand on metal-metal stretching frequencies can be seen by comparing the changes of ν(Rh-Rh) upon excitation of Rh(bridge) and $Rh_2(CNPh)_8^{2+}$: +65 vs. +102 cm^{-1}, respectively [37, 99]. (The force constant increases by 0.44 a 0.69 mdyn $Å^{-1}$, respectively.) The higher values for $Rh_2(CNPh)_8^{2+}$ indicate greater strengthening of Rh-Rh bonding when the metal atoms are unconstrained by the bridging ligand.

When experimental techniques combining UV or visible pulsed laser excitation with X-ray probing made it possible to study excited-state structures directly, d^8-d^8 systems quickly became testbeds for these new methods as the presence of heavy atoms, high photostability (photoreversibility), and long triplet lifetimes greatly aided data collection and analyses. It was

no surprise that the first time-resolved optical pump / monochromatic X-ray probe diffraction [100] and X-ray scattering experiments involving a polyatomic molecule [95] were performed on Pt(pop).

A Pt-Pt bond contraction of 0.28(9) Å was determined from work on $(Et_4N)_3H[Pt(pop)]$ crystals at 17 K using 355 nm nanosecond laser pulsed excitation probed by diffraction of synchrotron-generated X-ray pulses 33 μs long [45]. This estimated bond contraction value is near that (0.24 Å) obtained from X-ray diffraction on $(Bu_4N)_4[Pt(pop)]$ crystals under continuous 442 nm irradiation at 54 K [101]. The structure of excited Pt(pop) in solution was determined by time-resolved X-ray scattering [95] and absorption (EXAFS, Figure 7) [71], which yielded Pt-Pt contractions of 0.24 and 0.31(5) Å, respectively. In both techniques, structural parameters together with percentage photoexcitation yields were varied until the best match between calculated and experimental data was achieved. X-ray scattering data obtained on an aqueous $K_4[Pt(pop)]$ solution at 100 ps and 1 μs after 2 ps, 267 nm excitation were corrected for terms arising from bulk- and solvation-shell solvent molecules that change upon excitation due to the temperature rise caused by excited-state energy dissipation. Changes in axial solvent coordination and specific solvation appeared to be negligible. EXAFS spectra of Pt(pop) in the $^3d\sigma^*p\sigma$ state were measured in ethanol over the first 150 ns after 390 nm laser pulsed excitation [71]. The best fit of the transient EXAFS spectrum (Figure 7) was obtained assuming a 0.31 Å Pt-Pt contraction and an unchanged distance between the two P_4 planes. This analysis would suggest that the Pt atoms move upon excitation inwards from the P_4 planes and the Pt-P bonds elongate by 0.010(6) Å. The experimentally determined Pt-Pt and Pt-P bond-length changes on going to the $^3A_{2u}$ state in Pt(pop) solutions are somewhat longer than the values

calculated by DFT in a MeCN solution: -0.196 and +0.005 Å, respectively [50] (Table 1). (It should be noted that the experimental values sensitively depend on several parameters, such as the excitation yield, which may be in error. Positions of lighter atoms and solvent molecules were not varied in the fitting procedure.) In addition to the EXAFS structural information, X-ray absorption spectra (XAS) in the XANES region (X-ray absorption near edge structure) report on changes in the electronic structure [71, 73]. Pt(pop) XAS was measured at the L_3 edge that corresponds to electron excitation from the Pt $2p_{3/2}$ core orbital. The main peak ("white line") in the ground-state spectrum is due to excitation into $5d_{x2-y2}$ orbitals that are Pt-P σ-antibonding and δ, δ* with respect to the Pt-Pt bond. The peak broadened upon excitation at its blue side presumably due to $2p_{3/2}\rightarrow 6s$ transitions and increased δ-δ* splitting at a shorter Pt–Pt distance. Most importantly, a new band at 11.574 eV, which was attributed to the $2p_{3/2}\rightarrow d\sigma^*$ transition, emerged below the absorption edge (Figure 7). This feature, which was not present in the ground-state spectrum (with dσ* fully occupied), is attributable to the $^3d\sigma^*p\sigma$ excited-state spectrum (dσ* hole).

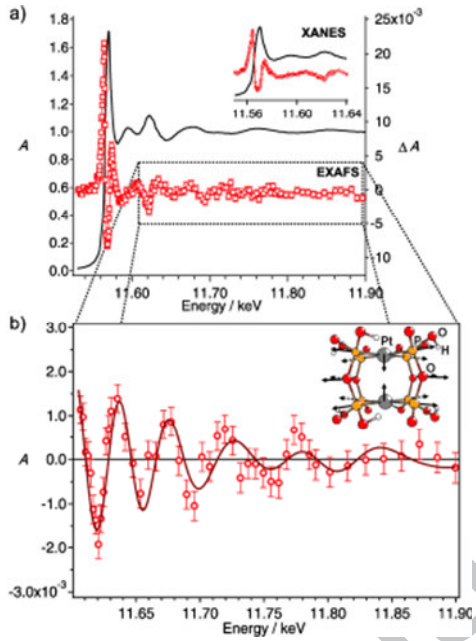

Figure 7. Static (black) and ^{3}dσ*pσ excited-state (red) X-ray absorption spectra of Pt(pop) in EtOH. The red spectrum was measured in a difference mode (excited – unexcited), integrated up to 150 ns after 100 fs, 390 nm excitation. Reproduced with permission from [71]. Copyright (2009) Wiley-VCH.

M(dimen) complexes (M = Rh, Ir) exhibit much larger metal–metal bond contraction than Pt(pop) upon dσ*pσ excitation. Rh(dimen) has a very shallow ground-state energy minimum [21] with a Rh–Rh distance of 4.50 Å measured on a [Rh(dimen)]$(PF_6)_2$·CH_3CN crystal at 17 K [102]. The Rh-Rh bond contracts to 3.64(5) Å upon 355 or 532 nm excitation, as determined by time-resolved X-ray diffraction [102]. The observed bond shortening (0.86(5) Å) is much smaller than the DFT-calculated value (1.54 Å), a discrepancy presumably caused by restrictive crystal packing forces. (It should be noted that the Rh(dimen) unit rotates in the crystal by 13° upon excitation.) Ir(dimen) is even more interesting, as two deformational isomers are present in solution (long/eclipsed and short/twisted, see above and ref. [21]) with Ir–Ir distances of 4.3(1) and 3.60(9) Å, respectively, determined by X-ray scattering in MeCN

[72]. Femtosecond pulsed laser excitation at 390 nm localizes the structure into a single short/twisted conformation with Ir-Ir distances of ~2.93(2) Å in ^{1}dσ*pσ and 2.90(2) Å in ^{3}dσ*pσ excited states (MeCN solution, time-resolved X-ray scattering [72]). For the triplet state, this corresponds to 0.7 and 1.4 Å Ir–Ir contractions relative to the short/twisted and long/eclipsed ground-state isomers, respectively. Another X-ray scattering study with femtosecond time resolution [75] determined the Ir–Ir distance in ^{1}dσ*pσ as 2.95(5) Å and the twist angle increase by 15(3)° relative to the long/eclipsed ground-state isomer. In combination with QM/MM calculations, the experiment also indicated that MeCN preferentially solvates the Ir atoms in the excited state through the *N*-end [75] with an Ir-NCMe distance of around 3 Å, whereas Ir···MeCN orientation is preferred in the ground state. Comparing the two classes of complexes, Pt(pop) and M(dimen), we note that the largest metal-metal contractions occur when there is a sufficiently flexible bridging ligand. The cage of four pop ligands, which places the two metal atoms at a much shorter ground-state distance than diisocyanide ligands, restricts structural changes caused by dσ*→pσ excitation – a conclusion that was drawn above from Raman data.

Deeper insight into electron density redistribution and origins of the structural changes upon dσ*→pσ excitation was obtained by excited-state DFT calculations on lowest excited singlet and triplet states of Pt(pop-BF_2), Ir(dimen), and Rh(bridge) [50, 70, 82, 90, 92]. Since singlet and triplet dσ*pσ excited states arise predominantly (≥95%) from dσ*→pσ (HOMO→LUMO) one-electron excitation, inspecting the (de)localization of these two orbitals is usually sufficient to understand the excited-state character. Since the HOMO is invariably an antibonding combination of metal (n-1)d_{z2} orbitals with ns and np contributions (Pt(pop-BF_2):

64% $5d_{z2}$, 14% 6s, 5% 6p [50]; short/eclipsed Ir(dimen) isomer: 56% $5d_{z2}$, 14% 6s, 18% 6p; long/eclipsed Ir(dimen) isomer 61% $5d_{z2,}$ 18% 6s, 15% 6p [82]; Rh(bridge): 56% $4d_{z2}$, 13% 5s) [92]), structural variations of excited-state character are mostly caused by variations in LUMO delocalization. In the case of Pt(pop) and Pt(pop-BF_2), the LUMO consists of ca. 43% $6p_z$ and 53-56% of pop-localized orbitals, (Figure 4). The dσ*pσ states have partial MMLCT character and the outward positioning of excited electron density at the PtP_4 faces could be of importance in excited-state reactivity [51, 52] and solvent interactions. (Note that the singly-occupied dσ* orbital also points out of the excited molecule along the Pt-Pt axis, Figure 4.) Excited electron density in isocyanide complexes is mostly distributed over the π_z*(C≡N) orbitals: 34-36% $5p_z$, 66% CN in Ir(dimen) [82]; 22% $4p_z$, 70% CN in Rh(bridge) [92]. dσ*⟶pσ excitation of isocyanide complexes thus involves pronounced charge transfer (MMLCT) to the C≡N groups, where the excited electron density distribution is anisotropic, oriented in the z-direction (parallel to the metal-metal axis). Accordingly, electron depopulation of Rh atoms in Rh(bridge) on going to the ^{3}dσ*pσ state was documented by DFT-calculations [92]; and the increased "π-back donation" was manifested experimentally by a ~16 cm^{-1} downshift of the C≡N stretching frequency [103]. (It is interesting to note the difference from the textbook case of π back donation. In dσ*pσ states, electron density is transferred to the π* ligand orbital from a metal np orbital, instead of the usual dπ-π* overlap.)

Experimentally documented metal–metal bond shortening has been qualitatively reproduced by many DFT calculations, optimizing the ^{3}dσpσ excited state in the gas phase [83, 90, 92] or solution [50, 70, 104]. The quantitative match with experimental values varies, depending on the functional, basis set, solvent model, etc. Most of the calculations also

correctly predict that metal-ligand bonds will be slightly lengthened. Recent DFT results on Pt(pop-BF_2) and Ir(dimen) are shown in Table 1. Metal-metal bond shortening in the ^{3}dσ*pσ state is accompanied by increasing bond order that reflects partial σ bond formation (Tables 2, 5).

Although excited-state potential energy surfaces have not been calculated for d^8-d^8 complexes (except Rh(dimen) in the gas phase [83]), it is reasonable to expect that the singlet and triplet dσ*pσ surfaces are nearly nested, as they have the same orbital origin. Indeed, nearly identical Pt–Pt bond-lengths were calculated [50] in singlet and triplet dσ*pσ states of Pt(pop) and Pt(pop-BF_2). Their minima are shifted to shorter metal-metal distances relative to the ground state (see above) and their shapes are more constricted because of higher stretching force constants. Essentially parabolic (harmonic) shapes of ground-state and dσ*pσ excited-state potential energy surfaces along the metal-metal coordinate are well established spectroscopically for Pt(pop), Pt(pop-BF_2), Rh(bridge), Rh(TMB) and Ir(TMB), usually by observing ν(M-M) progressions in absorption and/or emission spectra, with high vibrational quantum numbers (up to 20) occurring with equal spacing [35, 36, 42, 43, 58, 86]. (In some cases, the evidence also comes from symmetric spectral band shapes or observation of ν(M–M) Raman progression [7, 37, 99].) In contrast, Rh(dimen) and Ir(dimen) have strongly anharmonic ground- and excited-state energy surfaces (documented experimentally as well as computationally) [19, 21, 70, 74].

Large dσ*pσ singlet-triplet splittings (3000 - 3700 cm^{-1} for bridged Rh^I complexes [7, 19]; 5200-5400 and 5750 cm^{-1} for Pt(pop) and Pt(pop-BF_2), resp. [36, 42, 58]; 3450 and 5100 cm^{-1} calculated for long/eclipsed and short/twisted Ir(dimen), resp.) and energy separations

from higher-lying excited states are other photophysically relevant features. The gaps between $^1d\sigma^*p\sigma$ and the next higher state in Pt(pop) and Pt(pop-BF_2) were calculated [50] as 4200 and 5800 cm^{-1}, respectively. Even larger gaps (8-10000 cm^{-1}) can be estimated for Rh(TMB) and Ir(TMB) from their MCD spectra [94], ~11000 cm^{-1} for Rh(bridge) [7] and ~5600 cm^{-1} for Rh(dimen) [19]. A gap of 6020 cm^{-1} was calculated for Ir(dimen).

Table 3. Photophysical properties of selected d^8-d^8 complexes.

	τ_S	ϕ_{Fl}	τ_T	ϕ_{Ph}	Remarks	Ref.
Pt(pop) [a]	0.7 ps	1.5×10^{-4}	9.4 µs	0.61	in MeCN, 293 K	[42, 48]
	11.0 ps	-	-	-	DMF, 293 K	[42, 47]
	13.7 ps	1.6×10^{-4}	9.8 µs	0.52	H_2O, 293 K	
	25.6 ps	-	-	-	EtOH, 293 K, 293 K	
	30.3 ps	-	-	-	Ethylene Glycol, 293 K	
	53.8 ps (740)	-	-	-	1:2 H_2O:Glycerol, 293 K (80 K)	[46]
	66.4 ps (1860)	-	-	-	1:2 D_2O:*d*3-Glycerol (80 K)	
	44.1 ps (850)	-	-	-	4:1 EtOH:MeOH	
	46.3 (1900)	-	-	-	4:1 EtOD:MeOD	
	18.4 ps (660)	-	-	-	2-MeTHF/EtCN	
	101.5 ps (620)	-	-	-	PMMA film (80 K)	
Pt(pop-BF_2) [a]	1.6 ns τ_{ISC}=2.1 ns [h]	0.27	8.0 µs	0.49	in MeCN, 293 K	[57]
Rh(bridge) [b]	1.3 ns	0.07	8.3 µs	0.32	~295 K, 2MeTHF/EtCN, τ_{Fl} in MeCN	[7, 15]
	-	0.08	12.5 µs	0.6	77 K, 2MeTHF/EtCN	
Rh(TMB) [b]	900 ps	0.055	30 ns	$\sim10^{-3}$	~295 K, 2MeTHF/EtCN, τ_{Fl} in MeCN, EtOH/MeOH or PMMA	[7, 8, 19]
	820 ps				MeCN, room T	
	1.4 ns	0.09	20.5 µs	0.5	77 K, 2MeTHF/EtCN, τ_{Fl} in EtOH/MeOH or PMMA (1.8 ns)	
Rh(dimen) [c]	230 ps	0.0016	<1 ns	$<10^{-4}$	295 K, 2MeTHF/MeCN, τ_{Fl} in PMMA, ϕ_{Fl} is exc.-wavelength dependent	[19]
	1.5 ns	0.016	21 µs	0.17	77 K, 2MeTHF:MeCN, τ_{Fl} in PMMA	
Ir(dimen) [c]	63	-	0.41 µs	-	MeCN, room T	[72]
Ir(pz)(CO)(cod) [d]	<20 ps	$\sim10^{-4}$	0.25 µs	7.8×10^{-3}	295 K, MeCN, τ_{fl} in cyclohexane 1,2-$C_2H_2Cl_2$ enhances ISC	[8, 10, 105]
	-	-	2.68 µs	-	77 K, MeCN	[10]

Ir(pz*)(CO)$_2$ [e]	~100 ps	0.0051	3.3 μs	0.096	300 K, 2-Methylpentane	[9]
			10.9 μs		77 K	
Ir(pz*)(CO)(PPh$_2$OCH$_2$CH$_3$) [f]	100 ps	0.0023	1.1 μs	0.025	MeCN, room T	[11]
[Pt(μ-pz')(ppy)]$_2$ [g]	145 fs	-	0.85 μs	0.03	toluene, room T	[66]

[a] Bu_4N^+ salts; [b] PF_6 or O_3SCF_3 salts; [c] PF_6 salt; [d] Ir_2(μ-pyrazolyl)$_2$(1,5-cyclooctadiene)$_2$ (Fig. 2); [e] Ir_2(μ-3,5-Me$_2$-pyrazolyl)$_2$(CO)$_4$; [f] [Ir_2(μ-3,5-Me$_2$-pyrazolyl)$_2$(CO)$_2$(PPh$_2$OCH$_2$CH$_3$)$_2$ (Fig. 2); [g] Pt_2(μ-3,5-^{t}Bu$_2$-pyrazolyl)$_2$(2-phenylpyridine)$_2$ (Fig. 14); [h] Because of large ϕ_{fl}, the nonradiative decay lifetime τ_{ISC} differs from total decay lifetime.

Table 4. Temperature dependence of ^{1}dσ*pσ excited-state decay kinetics. Parameters were obtained by fitting nonradiative decay rate constants to a 2-channel equation [46] $k_{ISC} = k_o + (A/(\sqrt{k_BT}))\exp(-E_a/k_BT)$.

	k_{ISC} (s^{-1}) [a]	k_o (s^{-1})	A ($s^{-1}cm^{1/2}$)	E_a (cm^{-1})	Remarks	Ref.
Pt(pop)	1.4×10^{12}	-	-	-	~294 K, MeCN	[48]
	5.4×10^{10}	1.5×10^{9}	2.6×10^{14}	1190	2-MeTHF/EtCN	[46]
	1.9×10^{10}	1.5×10^{9}	6.0×10^{14}	1590	1:2 H_2O:Glycerol, 293 K	
	1.5×10^{10}	5.8×10^{8}	2.7×10^{15}	1930	1:2 D_2O:*d*3-Glycerol	
	2.3×10^{10}	1.3×10^{9}	2.2×10^{14}	1340	4:1 EtOH:MeOH	
	2.2×10^{10}	6.3×10^{8}	3.7×10^{14}	1450	4:1 EtOD:MeOD	
	9.9×10^{9}	1.7×10^{9}	9.2×10^{12}	890	PMMA film	
Pt(pop-BF_2)	4.7×10^{8}	8.5×10^{7}	3.0×10^{14}	2230	MeCN	[57]
	7.6×10^{8}	3.4×10^{7}	1.9×10^{13}	1600	solid	[58]}
			5.6×10^{10}	450		
Rh(bridge)	7×10^{8}	-	-	-	2-MeTHF/EtCN	[7]
Rh(TMB)	1.1×10^{9}	7.2×10^{8}	1.0×10^{12}	1070	4:1 EtOH:MeOH	[7]
	1.2×10^{9}	7.0×10^{8}	1.6×10^{12}	1110	4:1 EtOD:MeOD (E_a in PMMA : 1110 cm^{-1})	
Rh(dimen) [b]	4.5×10^{9}	6.8×10^{8}	8.6×10^{12}	1030	PMMA	[19]

[a] At 293 – 300 K. [b] Data were fitted to $k_o + A'\exp(-E_a/k_BT)$ [19]. The A' value was converted to A by multiplying by 14.27 $cm^{1/2}$ (T = 293 K).

4. Excited states: photophysics

*4.1. ^{1}dσ*pσ lifetimes and intersystem crossing*

The $^1d\sigma^*p\sigma$ states have lifetimes in the pico-nanosecond range (Table 3) that are much longer than those (femto-picosecond range) of most transition metal complexes [66, 106-119]. $^1d\sigma^*p\sigma$ states decay radiatively to the ground state and nonradiatively to the lowest triplet ($^3d\sigma^*p\sigma$). The rate of intersystem crossing (ISC) to $^3d\sigma^*p\sigma$ is solvent-, temperature-, and structure- dependent [7, 19, 46-48, 57, 58]. The most striking example of the latter is the dramatic increase in the $^1d\sigma^*p\sigma$ lifetime (~2290×) and fluorescence yield upon perfluoroboration of Pt(pop) to Pt(pop-BF_2) (Table 3) [57].

For symmetry reasons, first-order spin-orbit coupling (SOC) between $^1d\sigma^*p\sigma$ and $^3d\sigma^*p\sigma$ is forbidden, while large energy gaps to higher states limit 2nd order (indirect) SOC. As a result, $^1d\sigma^*p\sigma$ and $^3d\sigma^*p\sigma$ are nearly pure singlets and triplets (96 and 98% singlet and triplet character, respectively, was calculated [50] for Pt(pop) and Pt(pop-BF_2)). The ISC rate, which is nearly temperature independent up to 80-100 K, increases exponentially at higher temperatures (Table 4). Such temperature dependence is usually interpreted in terms of a two-pathway model consisting of slow direct ISC along with a thermally activated pathway [7, 19, 46, 58]. Considering the large singlet-triplet energy gap and nearly nested potential energy surfaces, the direct pathway can be explained by weak coupling [120] to higher vibrational levels of the triplet. The small SO coupling between singlet and triplet $d\sigma^*p\sigma$ states could arise from second-order interactions via high-lying E_u states of partial $p\pi p\sigma$ and $d\pi p\sigma$ character predicted by SO-TDDFT calculations [50]. The activated ISC pathway was originally interpreted [46] as thermal population of a higher-lying intermediate triplet state that would undergo ultrafast conversion to the lowest triplet ($^3d\sigma^*p\sigma$). The activation barrier would then correspond to crossing between $^1d\sigma^*p\sigma$ and intermediate-state potential energy surfaces (i.e.,

the high-temperature limit of a quantum mechanical nonradiative transition between two strongly coupled states [120], see also ref. [46]). However, experimental activation energies (Table 4) are much smaller than the energy gaps between ^{1}dσ*pσ and any of the higher triplet states (5670 and 3810 cm^{-1} for Pt(pop-BF_2) and Pt(pop), respectively, at the optimized ^{1}dσ*pσ geometry [50]). Still, an intermediate state could be present, provided that its energy falls sharply along a coordinate that is not coupled to the spectroscopic dσ*pσ singlet and triplet transitions (and, hence, not observed in the vibronic structure of emission or absorption spectra). A crossing between ^{1}dσ*pσ with such a state could then occur along this ISC-active coordinate even if the vertical energy gap at the ^{1}dσ*pσ minimum is too large. Evidently, vibrational activation along this coordinate would be needed to bring the excited molecule to the state-crossing region. In fact, some kind of distortion is the basis of all alternative explanations of the temperature-activated ISC pathway considered so far. In general, it can be assumed that ^{1}dσ*pσ $\rightarrow$ ^{3}dσ*pσ ISC requires a structural (vibronic) distortion that either makes the two states directly SO-coupled by symmetry lowering or transiently brings down a higher-lying excited state (presumably of ^3E_u origin with a pπpσ or, better, a dπpσ component) that can mediate ISC either by enhancing 2nd-order SOC between dσ*pσ singlet and triplet states or by acting as an intermediate [47, 48, 50, 57, 58]. For example, an antisymmetric twist around the metal-metal bond would disrupt π-interaction and decrease the energies of pπpσ and dπpσ excited states. More extensive transient distortions also involving fluctuating interactions between the excited binuclear complex and solvent molecules that would temporarily destroy the symmetry between the two metal centers and mix electronic states were recently indicated by QM/MM simulations of Pt(pop) in MeCN [48]. Such distortions would lead to large

fluctuations in excited-state energies and frequent energy crossings between the lowest excited dσ*pσ singlet and the second triplet that in turn could provide an ultrafast ISC pathway. In this model, experimental activation energies do not correspond to energy gaps between ^{1}dσ*pσ and upper intermediate states but, instead, to energies required to reorganize ^{1}dσ*pσ-excited systems (the binuclear complex + solvent molecules + counterions) to ISC-active configurations. Or, it may be argued that higher temperatures enhance structural fluctuations and increase the frequency of populating ISC-active configurations that is directly related to the ISC rate. Faster ISC would then be expected for structurally more flexible d^8-d^8 molecules; and, note that the fluorescence lifetime decreases and the nonradiative decay rate constant k_{ISC} increases (Tables 3, 4) on going from Rh(bridge) to Rh(TMB) and Rh(dimen) [7, 19]. Even more pronounced is the change in the ISC rate upon perfluoroboration of Pt(pop) to Pt(pop-BF_2) in MeCN, where k_{ISC} drops ~3000-times [48, 57] as the structural rigidity increases, owing to covalent BF_2 links between pop ligands. Moreover, energy gaps between ^{1}dσ*pσ and higher states are larger in Pt(pop-BF_2) [50], which also would disfavor ISC. (More extensive structural distortions/fluctuations would be required if the coupling/intermediate states lie high in energy.) The solvent dependence of the Pt(pop) ISC rate [46-48] (Table 3) supports this hypothesis, since the ISC rate decreases as the energy gap between the ^{1}dσ*pσ absorption band and the first UV band increases [46, 48]. It also appears that the ISC rate is faster in low-viscosity media, which may be related to solvent-induced structural fluctuations.

The ISC rate has been measured in microcrystalline $(Bu_4N)_4$[Pt(pop-BF_2)] over a very broad temperature range 5 – 310 K [58]. The fluorescence lifetime and k_{ISC} were found to be

nearly temperature-independent up to ca. 80 K (3.2-3.1 ns; 3.7-3.6×10^7 s^{-1}), followed by a smooth rise at higher temperatures (Figure 8).

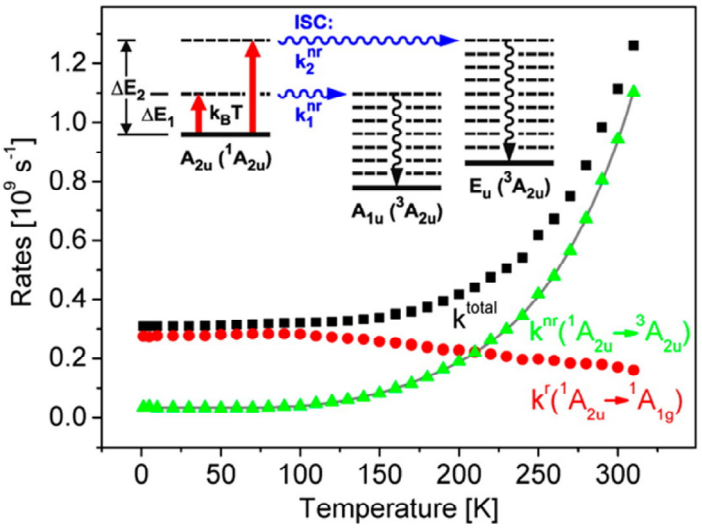

Figure 8. Temperature dependence of the ^{1}dσ*pσ nonradiative (ISC, green), radiative (red), and total (black) decay rate of solid $(Bu_4N)_4[Pt(pop\text{-}BF_2)]$. Inset: proposed ISC mechanism. Reproduced with permission from ref. [58]. Copyright (2016) American Chemical Society.

The temperature dependence of k_{ISC} was fitted over the 5 – 310 K range to a Boltzmann-type equation assuming a temperature-independent direct ISC due to weak ^{1}dσ*pσ - ^{3}dσ*pσ coupling along with two thermally-activated processes with activation energies of 450 and 1600 cm^{-1} (Table 4) that were tentatively attributed to separate pathways leading to the A_{1u} and E_u spin-orbit components of the ^{3}dσ*pσ state, likely involving multiphonon activation and spin-vibronic interactions [58]. The observed Boltzmann-like behavior indicates an important role for low-frequency phonons in promoting ISC. Further physical insight into this type of ISC temperature dependence could be obtained [121] by treating it as a vibrationally activated quantum-mechanical nonradiative process [46, 89, 120]. Acceptable fits to the $Pt(pop\text{-}BF_2)$ data using equations based on the Fermi Golden Rule required the presence of an intermediate

excited state energetically close to the $^1d\sigma^*p\sigma$ state [121]. As was discussed above, the energy of such a state would have to decrease rapidly along the normal coordinate corresponding to the activating vibration.

It is worth noting that different ISC models proposed so far point in the same direction: a thermally induced distortion that brings the singlet-excited d^8-d^8 species to a configuration where ISC is activated either by enhanced SOC or by crossing involving an intermediate state. Such distortion could be caused by solvent fluctuations, low-frequency phonons, and/or skeletal vibrations, depending on particular conditions.

4.2. $^3d\sigma^*p\sigma$ decay mechanism

Weak SOC with high-lying E_u singlets splits the $d\sigma^*p\sigma$ triplet state to higher E_u and lower A_{1u} SO states (sublevels). Zero-field splitting (zfs) values were determined by measuring phosphorescence lifetimes at low temperatures, where Boltzmann populations of the individual SO states are temperature-dependent. Values of 41-50 and 40 cm^{-1} were obtained for Pt(pop) [35, 36, 38, 41] and Pt(pop-BF_2) [58], respectively. A smaller zfs of about 11 cm^{-1} was determined for Rh(bridge) [122]. In general, zfs in the lowest triplet is too small to influence experimental results obtained above ca. 120 K, where equal population of all SO states can be assumed. E_u phosphorescence is symmetry-allowed through ca. 1% admixture of higher singlets [50]). On the other hand, phosphorescence from A_{1u} is symmetry forbidden. Still, phosphorescence from A_{1u} can be activated by simultaneous excitation of a vibrational mode of e_g symmetry ($A_{1u}\otimes E_g = E_u(x,y)$). (This is in D_{4h} core symmetry. b_g is the equivalent mode in C_{2h}.) Lifetimes of the E_u (4.5 μs) and A_{1u} (8.6 ms) triplet sublevels of Pt(pop-BF_2) differ by more than 3

orders of magnitude, reflecting the symmetry allowed and forbidden nature of their respective radiative decays [58]. The vibronic activation of A_{1u} radiative decay is manifested by the shift of the phosphorescence band by ~220 cm^{-1} to lower energy as the temperature drops below 10 K (and E_u emission frozen out), see Figure 9.

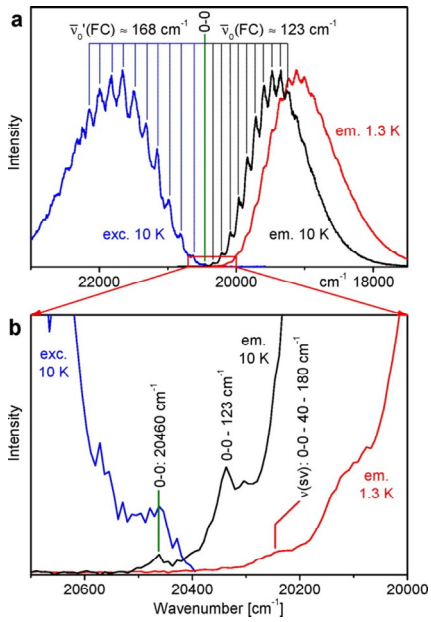

Figure 9. High-resolution phosphorescence (black, red) and excitation (blue) spectra of solid $(Bu_4N)_4[Pt(pop\text{-}BF_2)]$ measured at 10 and 1.3 K. 0–0 – 40 – 180 cm^{-1} in the lower (enlarged) figure denotes the false phosphorescence origin of the $A_{1u} \leftrightarrow A_{1g}$(ground state) transition that is shifted by 220 cm^{-1} to lower energy with respect to the $E_u \leftrightarrow A_{1g}$ 0–0 transition (at 20460 cm^{-1}), see the text. Reproduced with permission from ref. [58]. Copyright (2016) American Chemical Society.

Of this shift, 40 cm^{-1} is due to zfs and the remaining 180 cm^{-1} is the energy of the promoting vibration. Indeed, several e_g (b_g) deformation modes were identified [58] by Raman spectroscopy and DFT calculations in the 120 – 200 cm^{-1} range. The same behavior was found for Pt(pop) whose E_u and A_{1u} SO states have lifetimes of 1.58 and 880 µs, respectively, [35] and

A_{1u} radiative decay is promoted by a ~200 cm^{-1} vibration [35, 38, 41, 43]. This decay mechanism is expected to be general for d^8-d^8 complexes although the parameter values will differ.

Phosphorescence lifetimes and quantum yields for Pt(pop) [35, 38], Pt(pop-BF_2) [58] and Rh(bridge) [7] are nearly temperature independent above ca. 100 K, indicating that nonradiative decay to the ground state occurs primarily in the weak-coupling limit [120]. In contrast, Rh(dimen) [19] and Rh(TMB) [7] exhibit temperature-dependent phosphorescence lifetimes at higher temperatures that were interpreted in terms of a two-pathway model (a temperature-independent weakly coupled nonradiative transition along with an activated process). An activation barrier of 2610 cm^{-1} was determined for Rh(dimen) [19] in PMMA. Activation energies associated with Rh(TMB) phosphorescence decay were obtained from measurements in various media (in cm^{-1}): 3420 (PMMA), 2080 (DMF solution), 2660 and 2720 (H_2O and D_2O), 1970-2980 (solid, counterion-dependent) [123]. A linear correlation between the preexponential factor and activation energy was taken as confirmation that the decay mechanism is independent of the medium [123]. The finding that activated $^3d\sigma^*p\sigma$ decay occurs only for the two structurally flexible Rh-isocyanide dimers suggests that the activation process involves structural reorganization of the triplet state that would lead to surface crossing with one of the ground-state conformers. This interpretation was further supported by a ~1000 cm^{-1} red shift of both fluorescence and phosphorescence of Rh(dimen) in EtOH glass upon melting at 165 K. It is likely that a similar process is responsible for the relatively short Ir(dimen) lifetime (410 ns at room temperature [72], although the temperature dependence has not been reported). Temperature-dependent phosphorescence decay also was found for

$Ir_2(\mu\text{-}pz)_2(COD)_2$, with activation energies in the 2300 – 2600 cm^{-1} range, depending on pyrazolyl bridge substituents (H, CH_3, CF_3) [10].

Temperature dependence of phosphorescence decay is accompanied by a pressure dependence [124]. $^3d\sigma^*p\sigma$ lifetimes of Rh(TMB) and Ir(pz)(CO)(cod) increase with increasing pressure, with activation volumes of +4.6 and +2.8 cm^3mol^{-1} in MeCN. These increases were interpreted [124] as evidence for a strong-coupling [120] decay mechanism whereby the excited molecules undergo expansive distortion to achieve a crossing point with the ground-state potential energy surface. On the other hand, very weak pressure dependence and small negative volumes of activation were determined [124] in MeCN for Pt(pop) (-0.2 cm^3mol^{-1}) and Rh(bridge) (-0.5 cm^3mol^{-1}), whose phosphorescence decays are temperature-independent. This observation agrees with the weak-coupling mechanism [120] that does not require a structural distortion.

4.3. Singlet and triplet excited-state properties and reactivity

The presence of long-lived singlet and triplet $d\sigma^*p\sigma$ excited states, which gives rise to the rare phenomenon of dual emission (fluorescence + phosphorescence), opened the way for direct probing of differences in the structures and reactivities of these two states of identical orbital origin but different spin multiplicity. Although d^8-d^8 complexes appear to be well suited for investigations of spin effects on photoreactivity [8, 11, 16, 97, 105], this area remains relatively unexplored. Thermodynamics is different for electron transfer reactions of singlet and triplet states. For example, Pt(pop-BF_2) is expected to be a stronger photooxidant in the $^1d\sigma^*p\sigma$ state than in $^3d\sigma^*p\sigma$, with excited-state reduction potentials of +1.57 and +0.86 V (vs. Fc^+/Fc),

respectively [61]. Singlet and triplet excited-state electron transfer reactivity was studied in the $Ir_2(\mu\text{-}3,5\text{-}Me_2\text{-pyrazolyl})_2(CO)_2(PPh_2OCH_2CH_2\text{-pyridinium-R})_2$ series, where intramolecular photoinduced electron transfer occurs from $^1d\sigma^*p\sigma$ as well as $^3d\sigma^*p\sigma$ states of the Ir_2 unit to the appended pyridinium acceptor [11]. Singlet excited-state reactions are clearly faster due to larger driving forces. Rates of singlet and triplet forward ET as well as of the back reaction were measured for various R groups; and the rate vs. driving force plot provided compelling experimental evidence for Marcus inverted behavior [11]. A theoretical study of this process, which stressed the role of structural fluctuations, also showed that the electronic coupling between the pyridinium acceptor and the singlet- and triplet-excited Ir_2 chromophore is similar [16]. Relevant to atom-transfer photoreactivity, 1,2-dichloroethane quenches the $d\sigma^*p\sigma$ singlet and triplet of $Ir_2(\mu\text{-pyrazolyl})_2(1,5\text{-cyclooctadiene})_2$ with rate constants of 3×10^9 and 7.3×10^5 $M^{-1}s^{-1}$, respectively [105]. However, this difference was later attributed to enhanced ISC in the presence of 1,2-dichloroethane [8].

4.4. Excited-state spectroscopy

In addition to dual emission (spontaneous fluorescence and phosphorescence), d^8-d^8 complexes exhibit stimulated emission (SE) from the $^1d\sigma^*p\sigma$ state. SE, as well as triplet and singlet $d\sigma^*p\sigma$ excited-state absorption (ESA), are observable by time-resolved pump-probe UV-vis spectroscopy. (SE and ESA are manifested by signals of opposite signs.) The $^1d\sigma^*p\sigma$ ESA of Rh(TMB) displayed a strong feature between 400 and 500 nm, whereas $^3d\sigma^*p\sigma$ was characterized by a broad, weak absorption extending from 350 to 750 nm [8, 125]. The strong singlet-specific band at ~440 nm was attributed to a $d\sigma^*\rightarrow p\sigma$ transition that produces a

doubly-excited $(p\sigma)^2$ state, which can exist only as a singlet [8]. On the other hand, Pt(pop) in ethylene glycol (τ_{ISC} = 30.3 ps) exhibited essentially the same broad ESA around 335 and 460 nm from early picosecond time delays until 140 ps [47], attributable to overlapping singlet (at early times) and triplet absorptions (the latter appeared to be slightly broader on the red side, toward 480 nm). Pt(pop) SE occurs at ca. 400 nm, and its decay allowed determination of $^1d\sigma^*p\sigma$ lifetimes as a function of solvent [47, 48]. Analysis of time-resolved spontaneous and stimulated Pt(pop) emission in different solvents revealed two periods of $^1d\sigma^*p\sigma$ vibrational relaxation (210-280 fs and 1.3-2.1 ps) [47]. Both spontaneous and stimulated emission signals exhibited harmonic oscillations that will be discussed below. Similar behavior was found [85] for Pt(pop-BF_2) in MeCN, where $^1d\sigma^*p\sigma$ shows SE at 393 nm and the main ESA feature at 442 nm that blue-shifts to 425 nm, broadens and loses about half its intensity on going to the $^3d\sigma^*p\sigma$ state. Both excited states display a series of much weaker bands in the visible range [85]. In the case of Ir(dimen) in MeCN, SE decay revealed a 63 ps $^1d\sigma^*p\sigma$ lifetime [72] and rich oscillation dynamics [70]. Pronounced Ir(dimen) ESA has not been observed in the visible range [70, 72], perhaps due to broad overlapping ground-state absorptions.

4.5. Vibrational coherence

Coherent vibrational oscillations in the $^1d\sigma^*p\sigma$ state were observed by fluorescence upconversion and time-resolved absorption (SE and ESA) for Pt(pop) (Figure 10) and Pt(pop-BF_2) [47, 48, 85], as well as for Ir(dimen) (SE only) [70]. Femtosecond pulsed laser excitation of Pt(pop) coherently excites ca. three vibrational levels, creating a wave packet that oscillates between classical turning points on the excited-state potential energy surface [47].

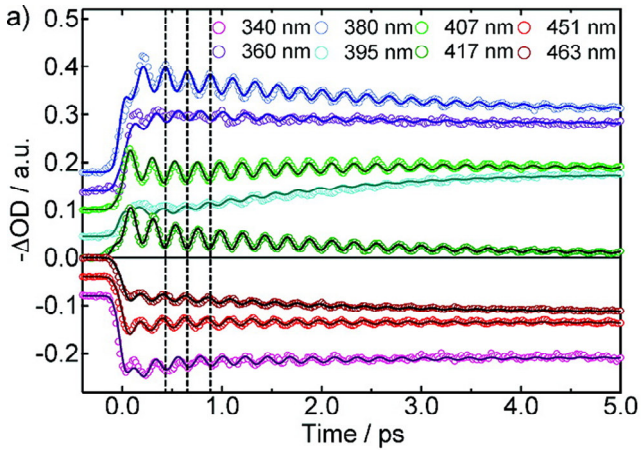

Figure 10. Kinetics traces obtained from time-resolved absorption spectra at fixed probe wavelengths following 370 nm excitation of Pt(pop) in ethylene glycol. Negative traces correspond to ESA, positive ones to ground-state bleach and SE. The vertical dashed lines help identify the π phase shift between the oscillations at the red and blue sides of the SE band (compare, e.g., 407 and 380 nm traces) that is characteristic of oscillations between classical turning points. Reproduced with permission from ref. [47]. Copyright (2011) American Chemical Society.

Oscillations with 224 and 281 fs periods and a 2.1 ps damping (decoherence) time were observed in ethylene glycol (Figure 10). Fourier transformation converted the oscillation periods into wavenumbers (149 and ~116 cm^{-1}) that can be assigned to excited- and ground-state ν(Pt–Pt) vibrations, respectively. (The latter oscillations, which are activated by a resonant impulsive stimulated Raman process in the ground state, were observed in the bleached ground-state absorption region.) The decoherence time (1.8-2.3 ps, depending on solvent) was much longer than depopulation of individual vibrational levels (~500 fs [47]). The surprisingly long-lived coherence was attributed [47] to the harmonic $^1d\sigma^*p\sigma$ potential along the Pt-Pt coordinate (virtually the only one undergoing change upon excitation, the vibrational frequency of a harmonic oscillator would not change during relaxation from the initially populated levels v = 6-9 toward v = 0). Similar behavior was observed for Pt(pop-BF_2) [85]. Current studies on

coherence transfer in singlet- and triplet-excited Pt(pop) in MeCN have led to deeper insight into the ISC mechanism [48].

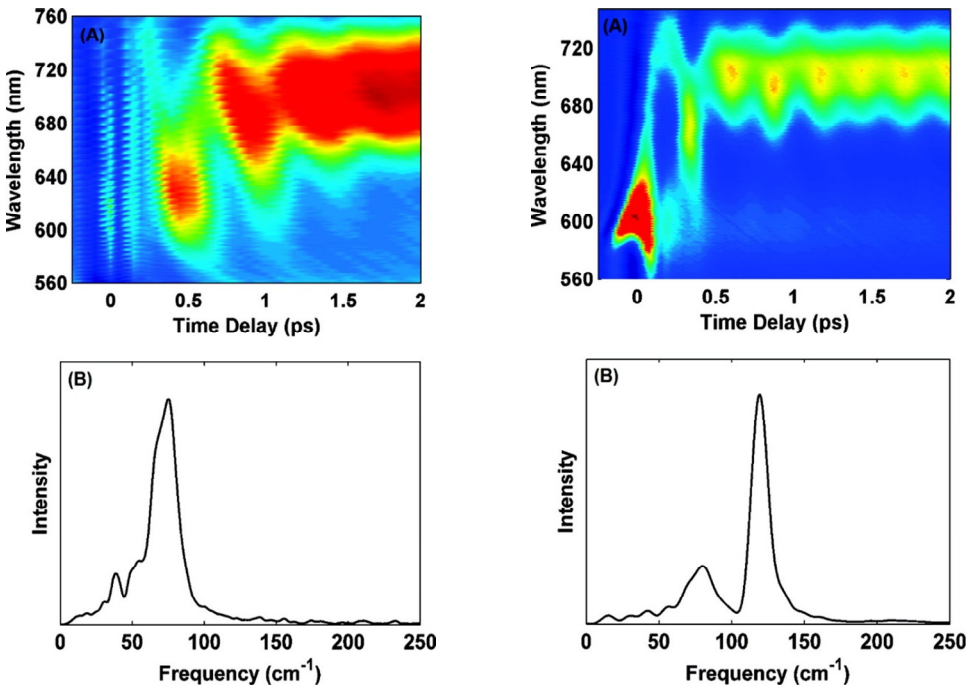

Figure 11. Top: time-resolved absorption spectra or Ir(dimen) in the SE region measured after 50 fs excitation of the long/eclipsed isomer at 477 nm (left) and the short/twisted isomer at 590 nm (right). Bottom: Fourier transforms of the oscillatory signal around 710 nm reveals the frequencies of contributing vibrations. Reproduced with permission from ref. [70]. Copyright (2011) American Chemical Society.

Ir(dimen) in MeCN shows an SE signal (Figure 11) whose oscillation pattern (but not the emission energy, 710 nm) depends on the excitation wavelength [70]. Exciting the long/eclipsed isomer with a 50 fs pulse at 477 nm creates a ν(Ir–Ir) wave packet (75 cm^{-1}), whereas excitation of the short/twisted isomer produces ν(Ir–Ir) and dihedral (C-Ir-Ir-C) twist wave packets oscillating at 80 and 119 cm^{-1}, respectively. Ground-state ν(Ir-Ir) oscillations at 11 and 48 cm^{-1} were observed in bleached ground-state absorption regions of the long/eclipsed and short/twisted isomers, respectively. This experiment clearly demonstrated the existence of two

different ground-state isomers that absorb at different wavelengths, while the observation of the same SE signal at both excitation wavelengths indicates that the $^1d\sigma^*p\sigma$ state has a single relaxed conformation. Further insight into Ir(dimen) excited-state ($^1d\sigma^*p\sigma$) dynamics was obtained from QM/MM calculations [74] on the long/eclipsed isomer in MeCN. Three oscillatory motions were identified, in which the whole population of excited molecules vibrates in phase: ν(Ir-Ir), twist, and ligand-breathing. The ν(Ir-Ir) frequency was calculated (70 cm^{-1}) near the experimental value [70] of 75 cm^{-1}. Unlike Pt(pop), the Ir(dimen) excited-state potential energy surface is anharmonic – much steeper on the short Ir-Ir side [21, 74]. Hence, the ν(Ir-Ir) frequency increases during vibrational relaxation as the potential becomes more harmonic near the energy minimum. Vibrational energy transfer (IVR) from ν(Ir-Ir) to the breathing mode was found to dominate at early times, quickly becoming hindered by the solvent [74]. Somewhat counterintuitively, it turns out that solvation facilitates ν(Ir-Ir) oscillations and sustains coherence. It was argued [74] that the most important solute-solvent interactions occur through ligands rather than Ir atoms. (This likely is the case also for Pt(pop), where the ligands could engage in H-bonding with solvent molecules [48].) The principal decoherence mechanism in Ir(dimen) was proposed [74] to be statistical, coming from a broad range of initial configurations. This mechanism contrasts with that proposed for Pt(pop), where decoherence is mostly dynamical, attributable to energy dissipation in each excited molecule [47, 48]. This difference highlights the importance of ligand rigidity in determining the structural/solvational distribution width of ground-state ensembles: narrow for Pt(pop) and Pt(pop-BF_2); broad for the much more flexible Ir(dimen).

4.6. Relaxation of higher excited states

Whereas fluorescence and phosphorescence excitation spectra and absorption spectra of Rh(bridge) and Rh(TMB) coincide in the $^1d\sigma^*p\sigma$ absorption region, the fluorescence excitation spectra are much weaker at shorter wavelengths, namely in the range of the sharp intense $d\pi\rightarrow p\sigma$ ^{1}MMLCT band at ~310 nm [7]. The same behavior was found for LMMCT bands of Pt(pop-BF_2) [48] (Figure 12). It follows that UV excitation into higher excited states triggers ultrafast relaxation processes that largely bypass the lowest excited singlet state ($^1d\sigma^*p\sigma$), directly populating the phosphorescent $d\sigma^*p\sigma$ triplet. A coherent evolution of UV-excited LMMCT states into the lowest $^3d\sigma^*p\sigma$ (and, in some cases also $^1d\sigma^*p\sigma$) was indicated by femtosecond UV-vis spectroscopy of Pt(pop) in H_2O and MeCN, and Pt(pop-BF_2) in MeCN [85]. For Rh(bridge), it was determined (Figure 13) [7] that the ^{1}MMLCT state (^1E_u) primarily decays (95%) to the corresponding ^{3}MMLCT (^3E_u) state (only 5% to $^1d\sigma^*p\sigma$). ^{3}MMLCT undergoes 88% internal conversion to $^3d\sigma^*p\sigma$ and 12% ISC to $^1d\sigma^*p\sigma$ ($^1A_{2u}$). Altogether, only ~17% of the initial excited ^{1}MMLCT population decays though the lowest excited singlet state ($^1d\sigma^*p\sigma$). In the case of Rh(dimen), part of the ^{1}MMLCT excited population decays directly to the ground state, bypassing both $d\sigma^*p\sigma$ singlet and triplet states [19].

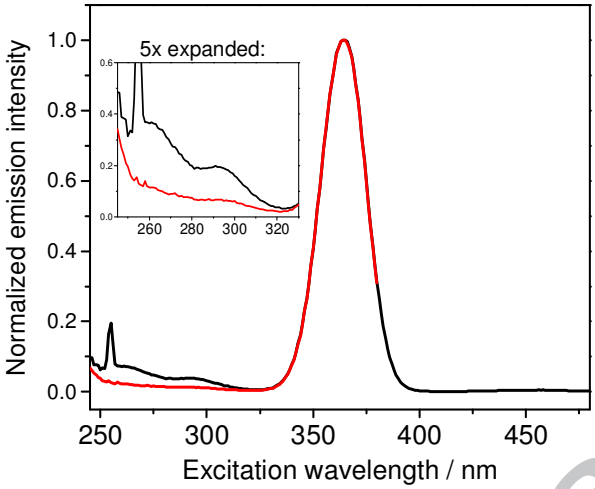

Figure 12. Fluorescence (red) and phosphorescence (black) excitation spectra of Pt(pop-BF_2) in MeCN at 294 K [this work]. The spectra are normalized at the $^1d\sigma^*p\sigma$ peak maximum (364 nm). To compare with the absorption spectrum, see Figure 5-bottom.

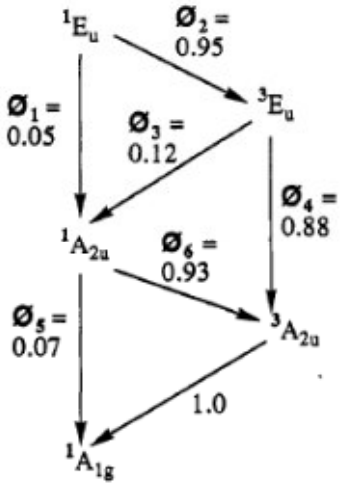

Figure 13. Excited-state conversions in Rh(bridge) at room temperature in MeCN. Reproduced with permission from ref. [7]. Copyright (1993) American Chemical Society.

This behavior of UV-populated states is typical for d^8-d^8 complexes, observed also for Rh(TMB), Ir(TMB), and Ir_2(μ-pyrazolyl)$_2$(CO)$_4$ [7, 9]. It is attributable to symmetry-allowed SO interactions between high-lying states (mostly ^1E_u) and $^3d\sigma^*p\sigma$ (A_{2u}). High-lying excited states

have mixed-spin character and different geometries than $^3d\sigma^*p\sigma$, so that their potential energy surfaces may approach (cross) each other. Electronic relaxation of UV-states may proceed through a series of conical intersections involving the manifold of predominantly triplet MMLCT (isocyanides) or LMMCT (pop) states, some of which are spectroscopically silent. However, because of large energy gaps between those states and $^{1,3}d\sigma^*p\sigma$, conversion of UV-states to $^3d\sigma^*p\sigma$ must occur at relatively high energies and geometries different from that of relaxed $^3d\sigma^*p\sigma$. (The same argument holds for minor pathways populating $^1d\sigma^*p\sigma$ and, for Rh(dimen), the ground state.)

Using valence-bond arguments, two zwitterionic singlet metal-to-metal CT excited states were predicted to occur at high energies (≤300 nm for Rh(bridge) and Rh(TMB)) [94]. These states arise from excitation of a 5d electron from one metal atom to the $6p_z$ orbital on the other, giving rise to $M^+M^- \leftrightarrow M^-M^+$ states ($M^+ = Rh^{II}$, Ir^{II} or Pt^{III}; $M^- = Rh^0$, Ir^0 or Pt^I). Although no clear-cut experimental evidence for such states in d^8-d^8 systems is available, it would be interesting to know whether polar $M^{\delta+}M^{\delta-}$ excited singlet states could be temporarily stabilized by solvent fluctuations, affecting the photophysics (ISC) or giving rise to unique singlet-state photochemistry.

4.7. Metal-metal to ligand charge transfer and ligand-centered excited states

Not all d^8-d^8 complexes have lowest singlet excited states of $d\sigma^*p\sigma$ character. Introducing a π-accepting 2-phenylpyridyl (ppy) ligand in complexes of the type $Pt_2(\mu\text{-}^tBu_2pz)_2(ppy)_2$ ($^tBu_2pz$ = 3,5-bis(*tert*-butyl)pyrazolate) changes the LUMO to π*(ppy), while the HOMO retains dσ* character. This situation gives rise to $d\sigma^* \rightarrow \pi^*$(ppy) MMLCT lowest singlet

and triplet excited states (Figure 14) [64-67]. Ligand-centered (LC) states are the lowest ones if the Pt-Pt interaction is very weak and dσ* occurs below π(ppy) orbitals [64, 68]. The ground-state Pt-Pt distance can be tuned by the pyrazolate substituents: the bulkier substituent, the shorter Pt-Pt distance. These compounds show strong long-lived phosphorescence and some of them are thermochromic and rigidochromic [64, 67, 126]. Their spectroscopic, photophysical, and electrochemical properties are broadly tunable by variations of the bridging and cyclometalated ligands [67]. Generally, fluid media and higher (room) temperatures support stronger Pt-Pt interactions, shift the MMLCT band to longer wavelengths and, in some cases, switch the character of the lowest excited state from LC to MMLCT.

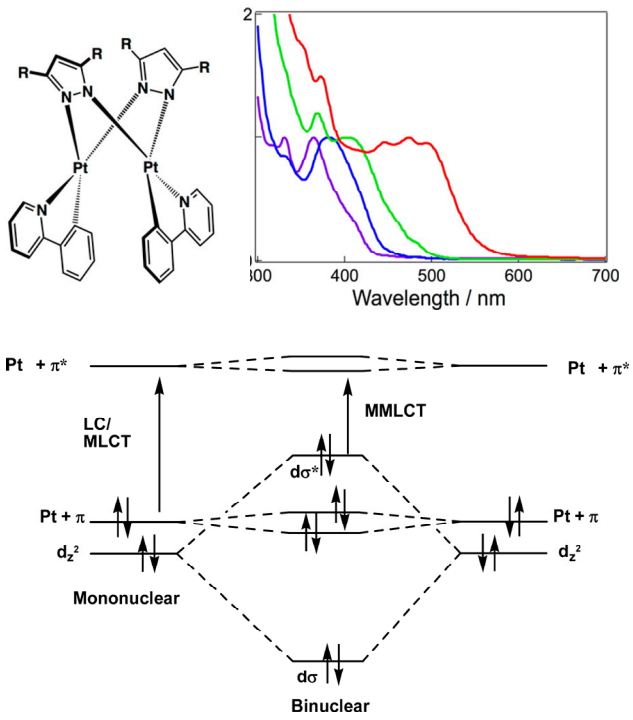

Figure 14. Structure of $Pt_2(\mu\text{-}3,5\text{-}R_2\text{-}pz)_2(ppy)_2$, absorption spectra as a function of R: H (violet); Me (blue); Ph (green); ^{t}Bu (red), and a qualitative MO diagram. Complexes with a long Pt-Pt distance have a lowest MLCT or ppy ligand-centered (LC) ππ* electronic transition localized at a single Pt center (left). Stronger Pt-Pt interactions increase the dσ* energy leading to an MMLCT lowest transition. The two upper levels correspond to in-phase and out-of-phase combinations of ppy π* orbitals. They are slightly split in energy because of interaction mediated by the Pt-Pt

bond. Reproduced with permission from refs. [68] and [67]. Copyright (2016, 2013) American Chemical Society.

In the case of $Pt_2(\mu\text{-}3,5\text{-}^tBu_2\text{-}pz)_2(ppy)_2$, a Pt-Pt bond shortening of ~0.2 Å on going to the ^{3}MMLCT state was estimated by time-resolved X-ray absorption (XANES) [65] while a larger value of ~0.5 Å and ppy ligand rotation are indicated by time-resolved X-ray scattering [69]. DFT calculations predict a Pt-Pt contraction ranging from 0.3 to 0.8 Å, depending on the bridging ligand [65, 68, 69, 127, 128]. Unlike complexes with a dσ*pσ lowest excited state, the Pt-Pt contraction upon MMLCT excitation is attributable predominantly to depopulation of the dσ* orbital, since the pσ orbital is not involved.

$Pt_2(\mu\text{-}^tBu_2pz)_2(ppy)_2$ shows remarkable coherence effects upon ^{1}MMLCT excitation with 510 nm laser pulses of ~50 fs duration [66]. Kinetics traces of polarized time-resolved absorption at 510 nm measured after excitation show oscillations that are π-shifted in the two polarizations (parallel and perpendicular to the excitation polarization), while oscillations were not observed in the trace measured at the magic angle. Oscillations persist until ca. 2 ps, which is longer than the ~145 fs ISC time. Their frequency changes sequentially. Oscillations start at 320 cm^{-1} and after 200 fs their frequency changes to 110 cm^{-1}. This unusual behavior was attributed to quantum beating between two electronic states resulting from excitation of a dσ* electron to the two π*(ppy) levels (see Figure 14). It was proposed that coherence is maintained through the ISC and the two oscillation frequencies (320, 110 cm^{-1}) were interpreted as double the values of the splittings (Figure 14-bottom) of ^{1}MMLCT and ^{3}MMLCT states, respectively. According to this interpretation, oscillations are of electronic origin, corresponding to flow of excited electron density from one ppy ligand to the other and back

[66]. Alternatively, the 110 cm^{-1} oscillation could originate from the excited-state Pt–Pt stretching mode [69]. This behavior should be investigated more thoroughly, as it could have far reaching implications for assisting photoinduced electron and energy flows.

4. Oxidized, reduced and superreduced states

Oxidation of d^8-d^8 complexes often is an irreversible 2-electron process promoted by axial coordination of Lewis bases (solvent molecules, halides, NCS^-, NO_2^-) [18, 20, 40, 60, 129]. The M-M bond shortens upon oxidative addition, for example from 3.243 Å in $Rh(bridge)^{2+}$ to 2.837 Å in $[Rh(bridge)Cl_2]^{2+}$ [129] or from 2.925 Å in Pt(pop) [33, 34] to 2.695 Å in $[Pt(pop)Cl_2]^{4-}$ [130]. Oxidized species are coordinatively saturated d^7-d^7 complexes with a full metal-metal single bond. Each complex exhibits a very intense $d\sigma \rightarrow d\sigma^*$ transition in the near UV spectral region whose energy depends on the extent of mixing between $d\sigma$ and axial-ligand σ orbitals [40, 104, 129]. A weaker absorption band, attributed to $d\pi \rightarrow d\sigma^*$ transitions, occurs at slightly lower energies, usually in the visible range [40, 129].

In contrast, $Ir_2(\mu\text{-}3,5\text{-}R,R'\text{-pyrazolyl})_2(1,5\text{-cyclooctadiene})_2$ (R,R' = H or Me) complexes undergo nearly reversible 1-electron oxidation in THF [131] or CH_2Cl_2 [132]. A second irreversible oxidation, which occurs in CH_2Cl_2 at more positive potentials, is facilitated by adding Lewis bases such as H_2O (moisture) or MeCN. A single two-electron reversible oxidation to a d^7-d^7 species with two axially coordinated MeCN molecules occurs in neat MeCN [132].

One-electron oxidized systems are primary products of oxidative quenching of $^3d\sigma p\sigma^*$ excited states, which is a common photoreaction of bridged Rh isocyanides [15], pyrazolyl-bridged Ir dimers [10, 11], Pt(pop) [49, 56] as well as Pt(pop-BF_2) [89]. Upon oxidative

quenching of *Rh(TMB) by methylviologen, a transient band attributable to $Rh(TMB)^{3+}$ was observed at 450 nm in MeOH (435 nm in MeCN) [15].

Triplet dσ*pσ states also are quenched by electron donors (e.g., aromatic amines) [15, 49, 56, 89], indicating formation of one-electron reduced species. Based on quenching and (in some cases) electrochemical experiments, ^{3}dσ*pσ excited-state reduction potentials were estimated as (vs. Fc^+/Fc, in MeCN): -0.1 V (*Rh(bridge) [15]), +0.7 V (*Pt(pop) [56]), and +0.86 V (*Pt(pop-BF_2) [61]). One-electron reduced products were detected by flash photolysis as short-lived intermediates: $Rh(bridge)^+$ and $Rh(TMB)^+$ exhibited broad absorption features at ~430 and ~750 nm [15]. For $Pt(pop)^{5-}$, very weak short-lived absorption around 400 nm was indicated by flash photolysis of $Pt(pop)^{4-}$ in the presence of *N,N*-dimethylaniline in MeOH [49]. Visible spectra of 1-electron reduced complexes were obtained by pulse radiolysis of Pt(pop) and Rh(TMB) in the presence of 1% *t*-butyl alcohol. Radiolysis-generated $Pt(pop)^{5-}$ in a phosphate buffer exhibited an intense peak at 420 nm and a weaker broad absorption at 580-600 nm that decayed with a 34 μs lifetime [133]. $Rh(TMB)^+$ (in MeCN) displayed bands at 740 and 570 nm, similar to those detected by flash photolysis upon reductive quenching. Reversible one-electron electrochemical reduction (as well as oxidation) was observed for Ir_2(μ-3,5-R_2-pyrazolyl)$_2$(1,5-cyclooctadiene)$_2$ complexes (R = H or Me); and electrochemiluminescence was detected upon cation/anion recombination [131]. (Electrochemiluminescence upon potential switching was seen also in the case of Pt(pop) that, however, shows neither reversible oxidation nor reduction [62, 63].)

Electrochemical and spectroelectrochemical detection of reduced d^8-d^8 complexes proved to be challenging, presumably owing to their high reactivity. Reduced complexes have

been generated electrochemically and characterized for Pt(pop-BF_2) [61] and Ir(dimen) [23]. Comparing the electrochemistry of these two systems has shed light on the effect of structural rigidity and LUMO delocalization on redox behavior. Pt(pop-BF_2) undergoes [61] chemically reversible and electrochemically quasireversible reduction at −1.68 V (vs. Fc^+/Fc), producing $[Pt_2(pop\text{-}BF_2)_4]^{5-}$ (abbreviated Pt(pop-BF_2)$^{5-}$). A second reduction, which occurs at −2.46 V (peak potential), yields superreduced Pt(pop-BF_2)$^{6-}$. The reaction is chemically reversible at 0° C but electrochemically irreversible, indicating structural reorganization that disfavors electron transfer at the electrode. The two reductions correspond to successive filling of the pσ orbital, creating very rare pσ bonds: $(p\sigma)^1$ bond in Pt(pop-BF_2)$^{5-}$ (Figure 15) and $(p\sigma)^2$ in Pt(pop-BF_2)$^{6-}$ (Figure 16). Pt atoms in the superreduced species have a $5d^8 6p^1$ electronic configuration (instead of the usual $5d^9$). This unique bonding model was supported by DFT calculations [61] that were validated by a good match of calculated and experimental UV-vis absorption and EPR spectra.

The extent of Pt–Pt bond strengthening upon reduction was estimated from Mayer−Mulliken bond orders (Table 2), which increase from 0.23 in the parent to 0.27 and 0.34 in the reduced and superreduced complexes, respectively; calculated Pt–Pt bond distances decrease from 2.901 to 2.815 and 2.740 Å (Table 1). We conclude that the rigid pop-BF_2 cage accommodates the $(p\sigma)^2$ bond in superreduced Pt(pop-BF_2)$^{6-}$, shielding it from the environment. The calculated Pt(pop-BF_2)$^{6-}$ structure is slightly distorted, whereby one pair of P–Pt–P angles on each side is larger than the other. However, the two Pt atoms are nearly equivalent electronically; their respective natural charges differ by only 0.035 e^- [61].

Of special interest are the changes in electronic absorption spectra along the Pt(pop-BF_2)^n redox series (Figure 17) [61], which can be explained using the qualitative MO diagram shown in Figure 3-left: Pt(pop-BF_2) exhibits the typical dσ*→pσ transition at 365 nm. Upon the first reduction, this band shifts to lower energy (416 nm); as the Pt–Pt interaction strengthens, the dσ* orbital is destabilized and pσ stabilized, decreasing the gap. A new weak spectral feature emerges at ~550 nm due to the pσ→LUMO+1 transition that cannot occur in the parent complex. The second reduction fills the pσ orbital. The dσ*→pσ transition disappears, being replaced by three weak bands due to transitions from pσ to higher unoccupied orbitals. (This qualitative model was supported by TDDFT calculations performed for each Pt(pop-BF_2)^n redox state [61].)

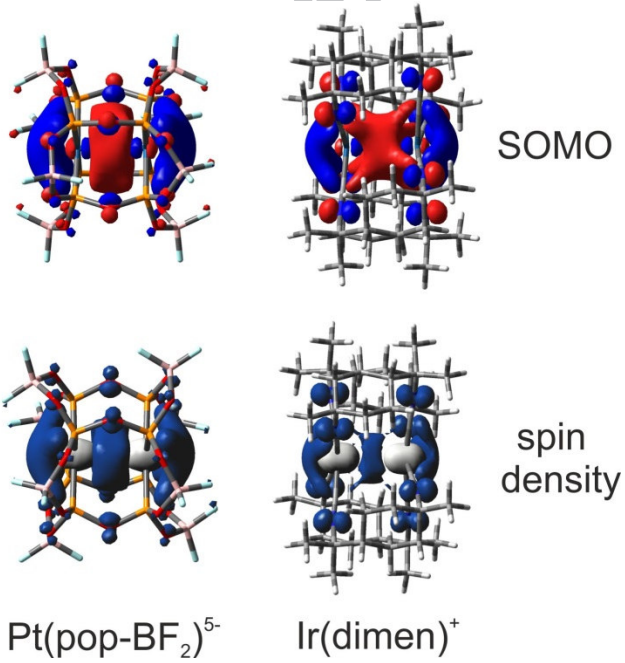

Figure 15. Calculated SOMO (top) and spin-density distribution (bottom) in 1-electron reduced d^8-d^8 complexes: left Pt(pop-BF_2)$^{5-}$; right, Ir(dimen)$^+$, both in MeCN solution. (DFT: PBE0/GD3/PCM-MeCN; this work).

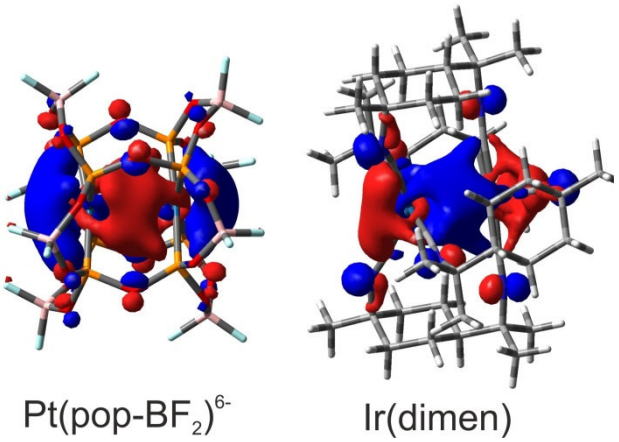

Figure 16. HOMO of superreduced $Pt(pop\text{-}BF_2)^{6-}$ (left) and twisted $Ir(dimen)^0$ (right) in MeCN [this work]. HOMO shapes are virtually identical for twisted and eclipsed $Ir(dimen)^0$ isomers. (DFT: PBE0/GD3/PCM-MeCN; this work)

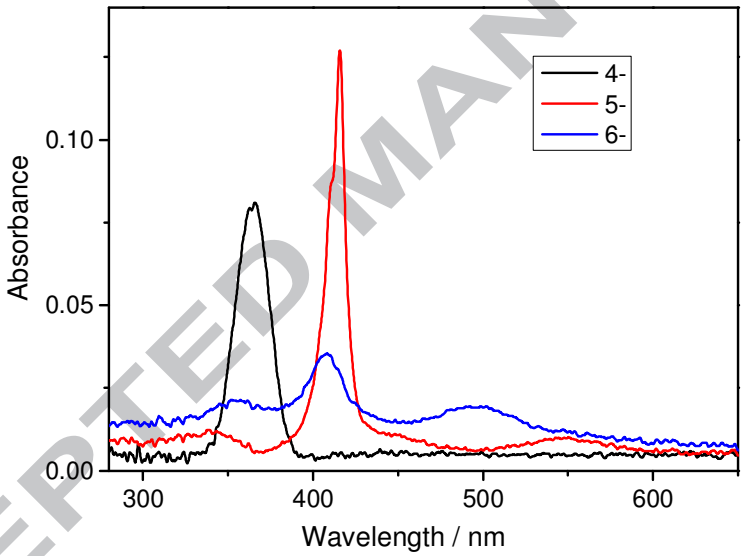

Figure 17. UV-vis absorption spectra of Pt(pop) (black), $Pt(pop)^{5-}$ (red) and superreduced $Pt(pop)^{6-}$ (blue) in MeCN. Measured spectroelectrochemically. (The intensity and shape of the ~408 nm feature are probably affected by overlap with a residual $Pt(pop)^{5-}$ 416 nm band due to incomplete reduction.) Reproduced with permission from ref. [61]. Copyright (2016) American Chemical Society.

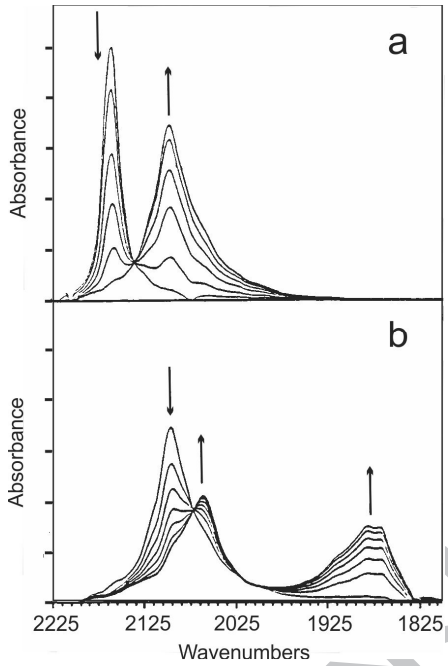

Figure 18. IR spectra recorded in the course of electrochemical reduction of Ir(dimen) in MeCN (containing 0.1 M Bu_4NPF_6). Top: the first reduction to $Ir(dimen)^+$, bottom: the second reduction to $Ir(dimen)^0$. Adapted with permission from ref. [23]. Copyright (1993) American Chemical Society.

Ir(dimen) undergoes successive 1-electron reductions at -1.34 and -1.53 V (vs. Ag/AgCl in 1 M KCl; approximately -1.7 and -1.9 vs. Fc/Fc^+), producing $Ir(dimen)^+$ and $Ir(dimen)^0$, respectively [23]. The infrared spectrum of Ir(dimen) [23] shows a single broad ν(C≡N) peak at 2156 cm^{-1} (Figure 18) that shifts by 66 cm^{-1} to lower wavenumbers upon the first reduction, owing to π-back donation from the pσ SOMO to π*(C≡N) orbitals that is clearly seen in the SOMO distribution (Figure 15). A more profound change of the ν(C≡N) IR spectral pattern occurs upon the second reduction to $Ir(dimen)^0$ whereby two downshifted features emerge at 2058 and 1869 cm^{-1} [23]. Such a large ν(C≡N) splitting indicates the formation of two kinds of C≡N– ligands in the superreduced molecule. One possible explanation assumes a loss of symmetry between the Ir centers in a mixed-valence $Ir^{I}\cdots Ir^{-I}$ (d^8-d^{10}) structure [23]. However,

DFT calculations indicate [82] that the two Ir atoms are nearly electronically equivalent and that the ν(C≡N) splitting originates from a *trans-cis* asymmetry between pairs of dimen ligands. The $Ir(CN–)_4$ units (that are almost planar in Ir(dimen) and $Ir(dimen)^+$) are heavily distorted in $Ir(dimen)^0$ toward a seesaw geometry with axial (nearly linear) NC–Ir–CN and equatorial (bent) $Ir(CN)_2$ units, see Figure 19-right. Two stable $Ir(dimen)^0$ conformations were calculated, which differ in the relative orientations of bent and linear NC–Ir–CN units at the two Ir centers but exhibit virtually identical ν(C≡N) vibrations. In both conformers, equatorial C≡N distances were calculated to be ~0.02 Å longer than axial ones and the corresponding Ir–C bonds are shorter by about 0.026-0.032 Å. The calculation predicted that the equatorial ligands would be bent at the N atoms (C≡N–C angles of ~145° vs. ~165° for the axial ligands). It follows that the second reduction would be largely localized at the equatorial C≡N– units, which is understandable in view of the extensive delocalization (64-68%) of the pσ HOMO over the ligands. In accord with this model, the Mayer-Mulliken Ir–Ir bond orders increase in each reduction reduction step (Table 5), similarly as in the case of $Pt(pop\text{-}BF_2)$ (Table 2). Mulliken charges on the two Ir atoms were calculated to be virtually identical and charge changes on corresponding C≡N– groups at each Ir center also are very similar (Table 6). The total charge change over the eight isocyanides (0.45-0.48 e^-) upon the second reduction is much larger than at the two Ir atoms (0.15-0.19 e^-). The electron density increases much more at the equatorial than axial ligands: 0.31-0.37 vs. 0.08-0.17 e^- (The two numbers are for different superreduced isomers, Table 6.) We conclude that superreduced $Ir(dimen)^0$ is another example of a $(p\sigma)^2$ dimer albeit with extensive delocalization over four of the C≡N– groups that induce the distortion of $Ir(C{\equiv}N–)_4$ moieties that in turn leads to the *trans-cis* asymmetry of C≡N– ligands. Interestingly, $Pt(pop\text{-}BF_2)^{6–}$ is

distorted in the same way but to a much smaller degree, as the extra electron density is more localized between the metal atoms (Figure 19).

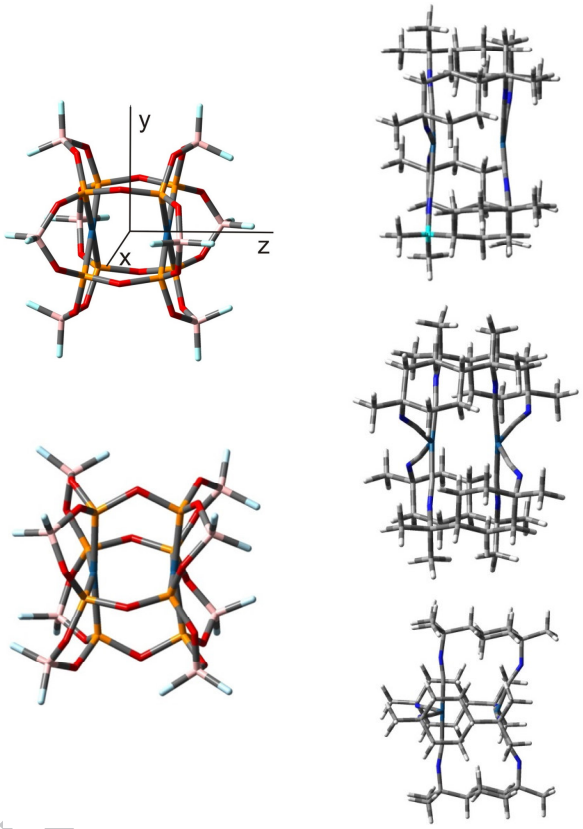

Figure 19. Left column: DFT-calculated structures of Pt(pop-BF_2) in MeCN (top) and superreduced Pt(pop-BF_2)$^{6-}$ (bottom). Right column: Ir(dimen) (top) and the two isomers of superreduced Ir(dimen)^0. [this work]

Table 5. Mayer-Mulliken bond orders for Ir_2(dimen)^n complexes, "short/twisted" isomer. (DFT: PBE0/GD3/PCM-MeCN, this work)

bond \ n	2+ long/eclipsed	2+ short/twisted	1+ [a]	0 twisted	0 eclipsed	2+ in ^{3}A exc. state
Ir – Ir	0.072	0.156	0.201	0.286	0.311	0.228
Ir – C1	0.525	0.558	0.618	0.594 [ax]	0.622 [ax]	0.653
Ir – C2	0.524	0.568	0.634	0.940 [eq]	0.928 [eq]	0.681
Ir – C3	0.523	0.559	0.618	0.594 [ax]	0.622 [ax]	0.625
Ir – C4	0.522	0.568	0.635	0.940 [eq]	0.928 [eq]	0.724

C1 – N1	2.374	2.345	2.237	2.170 [ax]	2.193 [ax]	2.124
C2 – N2	2.375	2.345	2.450	2.035 [eq]	2.038 [eq]	2.225
C3 – N3	2.375	2.345	2.237	2.170 [ax]	2.193 [ax]	2.126
C4 – N4	2.374	2.345	2.450	2.035 [eq]	2.038 [eq]	2.228

[a] No isomers found.

Table 6. Changes of DFT-calculated Mulliken charges upon the two reduction steps of Ir(dimen)^n. Isomers are specified in parentheses [this work].

	2(sh/tw)→1	1→0(tw)	1→0(ecl)
Ir1	-0.194	-0.072	-0.092
Ir2	-0.193	-0.074	-0.093
C_{ax}	-0.008	-0.012	-0.003
N_{ax}	-0.030	-0.031	-0.018
C_{eq}	-0.010	-0.035	-0.056
N_{eq}	-0.029	-0.042	-0.036

The much greater stability of reduced and superreduced Pt(pop-BF_2) as compared to the corresponding Pt(pop) states is likely caused by the lack of reducible hydrogen atoms as well as electron-withdrawing BF_2 groups that shield the Pt–Pt unit. On the other hand, the reduction products of Ir(dimen) are stabilized by π-back donation to C≡N– groups and by ligand flexibility that can accommodate structural changes induced by both reduction steps. It remains to be seen whether d^8-d^8 complexes can be employed as electrocatalysts. Preliminary results are encouraging: Ir(dimen)$^+$ and Pt(pop-BF_2)$^{5-}$ react with CH_2Cl_2 [23, 61]; and Ir(dimen)$^{2+}$ is an electrocatalyst for CO_2 reduction to formate and bicarbonate in a reaction cycle that involves CO_2 addition to superreduced Ir(dimen)^0 [134]. Residual water is reduced to H_2 in a parallel reaction. Given the predicted predominant localization of extra electron density in Ir(dimen)^0 at bent C≡N– groups, it is likely that their N atoms act as nucleophilic reaction centers. Perhaps

CO_2 reduction and H_2 formation involve an interplay between the ligand and metal sites in superreduced Ir(dimen)^0.

Conclusions

d^8-d^8 complexes exhibit common patterns of structural, spectroscopic, and photophysical behavior that stem from the presence of a σ-antibonding HOMO and a σ-bonding LUMO. This unique electronic structure gives rise to the signature $^1d\sigma^* \rightarrow p\sigma$ absorption band in the near UV (Pt-pop)) or visible (Ir, Rh di-isocyanides) spectral region, as well as to long-lived singlet (ps-ns) and triplet (μs) dσ*pσ excited states. The photophysics can be rationalized in terms of metal-metal-bond strengthening upon excitation, large singlet-triplet splittings, large energy separations between $^1d\sigma^*p\sigma$ and higher excited states, the absence of spin-orbit coupling between dσ*pσ singlet and triplet states along with nested and usually (except M(dimen)!) harmonic potential energy surfaces that are shifted to shorter metal-metal distances with respect to the ground state, and strong spin-orbit coupling among high-lying excited states of mixed-spin character that involve excitation from ligand-localized orbitals with pπ and dπ contributions (Pt(pop) and Pt(pop-BF_2)) or from predominantly dπ orbitals (diisocyanides) to the pσ LUMO, acquiring partial LMMCT and MMLCT character, respectively. A different electronic structure was found in complexes with terminal electron-accepting ligands of the type Pt_2(μ-pyrazolate)$_2$(ppy)$_2$ that feature a π*(ppy) LUMO and, hence, a (M)MLCT lowest excited state.

Differences in the behavior of Pt(pop)/Pt(pop-BF_2) and diisocyanide metal complexes can be explained by shorter metal-metal distances supported by the P–O–P bridging unit in the

former complexes and by LUMO (pσ) delocalization that is more extensive and confined to the π*(C≡N–) orbitals in the diisocyanides and spread over the outer PtP_4 regions (and also to some extent over the bridging oxygens) in Pt(pop)/Pt(pop-BF_2). The presence of C≡N– π electrons also gives rise to attractive dispersion interactions involving two parallel $M(C{\equiv}N{-})_4$ planes, stabilizing binuclear structures. Dispersion forces are less important in Pt(pop)/Pt(pop-BF_2).

Variations within the classes of d^8-d^8 complexes can be accounted for by the rigidity and bulkiness of the bridging ligand. The finding of a dramatically higher fluorescence quantum yield and longer $^1d\sigma^*p\sigma$ lifetime upon Pt(pop) perfluoroboration to Pt(pop-BF_2) is a case in point. Generally, ISC in d^8-d^8 systems requires thermally activated distortions and, hence, is facilitated by more flexible ligands and greater solvent accessibility. Among diisocyanide complexes, Rh(dimen) and Ir(dimen) appear to be the most structurally flexible.

Coherent oscillations of a ν(M-M) wave packet induced by femtosecond excitation into the $^1d\sigma^*\rightarrow p\sigma$ absorption band is a common feature of d^8-d^8 photophysics. Such oscillations were observed on harmonic as well as anharmonic $^1d\sigma^*p\sigma$ potential energy surfaces of Pt(pop)/Pt(pop-BF_2) and Ir(dimen), respectively, although with different decoherence mechanisms.

Electrochemical reduction often is irreversible, presumably because of the high reactivity of products and accompanying structural reorganization. Pt(pop-BF_2) and Ir(dimen) are exceptional cases that undergo two sequential 1-electron reductions; each step involves adding an electron to a pσ molecular orbital, which in the second step produces a rare $(p\sigma)^2$ metal-metal bond between (formally in each case) Pt^I and Ir^0 atoms. Superreduced $Ir(dimen)^0$ undergoes a structural distortion accompanied by localization of extra electron density on two

trans pairs of the C≡N– ligands, thereby causing bending at the N atoms. It will be of interest to see if such nucleophilic N-atoms interact with substrates (H^+, CO_2) in electrocatalytic processes.

We expect that future research on d^8-d^8 bridged as well as self-assembled systems will address fundamental questions such as ISC mechanisms, vibrational coherence and dephasing mechanisms (which will aid our understanding of energy flows in solvated molecular systems), and, importantly, differences in chemical reactivities of singlet and triplet excited states. And, in our view, both experimental and theoretical analyses of the mechanisms of photo- and electrochemical reactions catalyzed by d^8-d^8 complexes will continue to be very rich areas for exploration.

Acknowledgments
We thank our colleagues for interesting discussions of d^8-d^8 chemistry as well as sharing some (yet) unpublished data, most especially Majed Chergui, Ivano Tavernelli, Roberto Moni, and Gloria Capano (EFPFL, Switzerland); and Jay Winkler, Bryan Hunter, and Yan-Choi Lam (Caltech). This work was supported by the NSF CCI Solar Fuels Program (CHE-1305124), the Arnold and Mabel Beckman Foundation, the Ministry of Education of the Czech Republic - grant LH13015, and the COST Action CM1405.

Appendix: Computational details

The electronic structures Pt(pop-BF_2) and Ir(dimen) in various oxidation states and in the first triplet state were calculated by DFT using Gaussian 09 (G09) and ADF 2016.01 program packages. Open shell systems were calculated by the UKS approach, geometry optimization was followed by vibrational analysis in order to characterize stationary states. DFT calculations (G09) employed Perdew, Burke, Ernzerhof (PBE0) hybrid functional [135, 136], either alone or with the D3 version of Grimme's dispersion with the original D3 damping function added [137]. The solvent was described by the polarizable conductor calculation model (PCM) [138]. The following basis sets were used within G09: double-ζ 6-31g(d) basis set for H [139], polarized

triple-ζ basis sets 6-311g(d) for C, N, O, and P atoms [140, 141], and small-core quasirelativistic effective core pseudopotentials and corresponding optimized set of basis functions for Ir and Pt [142, 143]. Electronic transitions were calculated by time-dependent DFT (TDDFT). The methodology of spin-orbit TDDFT calculations using ADF program package has been described [144].

References

[1] G. Magnus, Pogg. Ann. 14 (1828) 239.
[2] M. Atoji, J.W. Richardson, R.E. Rund, J. Am. Chem. Soc. 79 (1957) 3017-3020.
[3] K.R. Mann, J.C. Gordon II, H.B. Gray, J. Am. Chem. Soc. 97 (1975) 3553-3555.
[4] V.W.-W. Yam, V.K.-M. Au, S.Y.-L. Leung, Chem. Rev. 115 (2015) 7589−7728.
[5] K.R. Mann, J.A. Thich, R.A. Bell, C.L. Coyle, H.B. Gray, Inorg. Chem. 19 (1980) 2462-2468.
[6] C.L. Exstrom, D. Britton, K.R. Mann, M.G. Hill, V.M. Miskowski, W.P. Schaefer, H.B. Gray, W.M. Lamanna, 35 (1996) 549-550.
[7] V.M. Miskowski, S.F. Rice, H.B. Gray, J. Phys. Chem. 97 (1993) 4277-4283.
[8] J.R. Winkler, J.L. Marshall, T.L. Netzel, H.B. Gray, J. Am. Chem. Soc. 108 (1986) 2263-2266.
[9] J.L. Marshall, M.D. Hopkins, V.M. Miskowski, H.B. Gray, Inorg. Chem. 31 (1992) 5034-5040.
[10] J.L. Marshall, S.R. Stobart, H.B. Gray, J. Am. Chem. Soc. 106 (1984) 3027-3029.
[11] L.S. Fox, M. Kozik, J.R. Winkler, H.B. Gray, Science 247 (1990) 1069-1071.
[12] R.S. Farid, I.-J. Chang, J.R. Winkler, H.B. Gray, J. Phys. Chem. 98 (1994) 5176-5179.
[13] K.R. Mann, N.S. Lewis, V.M. Miskowski, D.K. Erwin, G.S. Hammond, H.B. Gray, J. Am. Chem. Soc. 99 (1977) 5525-5526.
[14] I.S. Sigal, K.R. Mann, H.B. Gray, J. Am. Chem. Soc. 102, (1980) 7252-7256.
[15] S.J. Milder, R.A. Goldbeck, D.S. Kliger, H.B. Gray, J. Am. Chem. Soc. 102 (1980) 6761-6764.
[16] I.V. Kurnikov, L.D. Zusman, M.G. Kurnikova, R.S. Farid, D.N. Beratan, J. Am. Chem. Soc. 119 (1997) 5690-5700.
[17] K.R. Mann, H.B. Gray, Adv. Chem. Ser. 173 (1979) 225.
[18] M.R. Rhodes, K.R. Mann, Inorg. Chem. 23 (1984) 2053-2058.
[19] V.M. Miskowski, S.F. Rice, H.B. Gray, R.F. Dallinger, S.J. Milder, M.G. Hill, C.L. Exstrom, K.R. Mann, Inorg. Chem. 33 (1994) 2799-2807.
[20] P.D. Harvey, Coord. Chem. Rev. 219–221 (2001) 17–52.
[21] B.M. Hunter, R.M. Villahermosa, C.L. Exstrom, M.G. Hill, K.R. Mann, H.B. Gray, Inorg. Chem. 51 (2012) 6898−6905.
[22] K.R. Mann, B.A. Parkinson, Inorg. Chem. 20 (1981) 1921-1924.
[23] M.G. Hill, A.G. Sykes, K.R. Mann, Inorg. Chem. 32 (1993) 783–784.
[24] D.M. Roundhill, H.B. Gray, C.-M. Che, Acc. Chem. Res. 22 (1989) 55-61.
[25] D.C. Smith, H.B. Gray, Coord. Chem. Rev. 100 (1990) 169-181.
[26] R.J. Sweeney, E.L. Harvey, H.B. Gray, Coord. Chem. Rev. 105 (1990) 23-34.

[27] D.C. Smith, H.B. Gray, Atom-Transfer Reactivity of Binuclear d^8 Complexes, in: D.R. Salahub, M.C. Zerner (Eds.), ACS Symposium Series 394. The Challenge of d and f Electrons., American Chemical Society, Washington, DC, 1989, pp. 356-365.
[28] J.L. Marshall, A.E. Stiegman, H.B. Gray, Photochemistry of Dinuclear d^8-d^8 Iridium and Platinum Complexes, in: A.B.P. Lever (Ed.), Excited States and Reactive Intermediates. ACS Symposium Series., American Chemical Society, Washington, DC, 1986, pp. 166-176.
[29] A.P. Zipp, Coord. Chem. Rev. 84 (1988) 47-83.
[30] R.P. Sperline, M.K. Dickson, D.M. Roundhill, J.C.S. Chem. Comm. (1977) 62-62.
[31] A.D. Troitskaya, Trudy Kazan. Khim. Tekhnol. Inst. im. S.M. Kirova 23 (1957) 228.
[32] A.D. Troitskaya, Russ. J . Inorg. Chem. 6 (1961) 585.
[33] M.A. Dos Remedios Pinto, P.J. Sadler, S. Neidle, M.R. Sanderson, A. Subbiah, K. R., J. Chem. Soc., Chem. Comm. (1980) 13-15.
[34] R.E. Marsh, F.H. Herbstein, Acta Crystallogr., Sect. B 39 (1983) 280-287.
[35] W.A. Fordyce, J.G. Brummer, G.A. Crosby, J. Am. Chem. Soc. 103 (1981) 7061-7064.
[36] S.F. Rice, H.B. Gray, J. Am. Chem. Soc. 105 (1983) 4571-4575.
[37] C.-M. Che, L.G. Butler, H.B. Gray, R.M. Crooks, W.H. Woodruff, J. Am. Chem. Soc. 105 (1983) 5492-5494.
[38] J.T. Markert, D.P. Clements, M.R. Corson, J.K. Nagle, Chem. Phys. Lett. 97 (1983) 175-179.
[39] L. Bär, G. Gliemann, Chem. Phys. Lett. 108 (1984) 14-17.
[40] C.-M. Che, L.G. Butler, P.J. Grunthaner, H.B. Gray, Inorg. Chem. 24 (1985) 4662-4665.
[41] Y. Shimizu, Y. Tanaka, T. Azumi, J. Phys. Chem. 89 (1985) 1372-1374.
[42] A.E. Stiegman, S.F. Rice, H.B. Gray, V.M. Miskowski, Inorg. Chem. 26 (1987) 1112-1116.
[43] T. Ikeyama, S. Yamamoto, T. Azumi, J. Phys. Chem. 92 (1988) 6899-6901.
[44] L. Bär, H. Englmeier, G. Gliemann, U. Klement, K.-J. Jurgen Range, Inorg. Chem. 29 (1990) 1162-1168.
[45] N. Yasuda, H. Uekusa, Y. Ohashi, Bull. Chem. Soc. Jpn. 77 (2004) 933–944.
[46] S.J. Milder, B.S. Brunschwig, J. Phys. Chem. 96 (1992) 2189-2196.
[47] R.M. van der Veen, A. Cannizzo, F. van Mourik, A. Vlček, Jr. , M. Chergui, J. Am. Chem. Soc. 133 (2011) 305-315.
[48] R. Monni, G. Capano, G. Auböck, K.M. Lange, H.B. Gray, I. Tavernelli, A. Vlček, M. Chergui, Nat. Chem., submitted (2017).
[49] J.R. Peterson, K. Kalyanasundaram, J. Phys. Chem. 89 (1985) 2486-2492.
[50] S. Záliš, Y.C. Lam, H.B. Gray, A. Vlček, Jr., Inorg. Chem. 54 (2015) 3491−3500.
[51] A. Vlček, Jr., H.B. Gray, J. Am. Chem. Soc. 109 (1987) 286-287.
[52] A. Vlček, Jr., H.B. Gray, Inorg. Chem. 26 (1987) 1997-2001.
[53] E.L. Harvey, A.E. Stiegman, A. Vlček, Jr., H.B. Gray, J. Am. Chem. Soc. 109 (1987) 5233-5235.
[54] A.D. Kirk, L.-Z. Cai, Inorg. Chem. 37 (1998) 1051-1059.
[55] A.D. Kirk, L.-Z. Cai, Chem. Commun. (1997) 523-524.
[56] W.B. Heuer, M.D. Totten, G.S. Rodman, E.J. Hebert, H.J. Tracy, J.K. Nagle, J. Am. Chem. Soc. 106 (1984) 1163-1164.
[57] A.C. Durrell, G.E. Keller, Y.-C. Lam, J. Sýkora, A. Vlček, Jr., H.B. Gray, J. Am. Chem. Soc. 134 (2012) 14201−14207.
[58] T. Hofbeck, Y.C. Lam, M. Kalbáč, S. Záliš, A. Vlček, H. Yersin, Inorg. Chem. 55 (2016) 2441−2449.
[59] H.B. Gray, T. Hofbeck, Y.C. Lam, J.R. Winkler, H. Yersin, German Patent DE10 2014 111050A8 German Patent DE10 2014 111050A8
[60] S.A. Bryan, R.H. Schmehl, D.M. Roundhill, J. Am. Chem. Soc. 108 (1986) 5408–5412.
[61] T.V. Darnton, B.M. Hunter, M.G. Hill, S. Záliš, A. Vlček, Jr., H.B. Gray, J. Am. Chem. Soc. 138 (2016) 5699−5705.

[62] J. Kim, F.F. Fan, A.J. Bard, C.-M. Che, H.B. Gray, Chem. Phys. Lett. 121 (1985) 543-546.
[63] A. Vogler, H. Kunkely, Angew. Chem. Int. Ed. Engl. 23 (1984) 316-317.
[64] B. Ma, J. Li, P.I. Djurovich, M. Yousufuddin, R. Bau, M.E. Thompson, J. Am. Chem. Soc. 127 (2005) 28-29.
[65] J.V. Lockard, A.A. Rachford, G. Smolentsev, A.B. Stickrath, X. Wang, X. Zhang, K. Atenkoffer, G. Jennings, A. Soldatov, A.L. Rheingold, F.N. Castellano, L.X. Chen, J. Phys. Chem. A 114 (2010) 12780–12787.
[66] S. Cho, M.W. Mara, X. Wang, J.V. Lockard, A.A. Rachford, F.N. Castellano, L.X. Chen, J. Phys. Chem. A 115 (2011) 3990–3996.
[67] A. Chakraborty, J.C. Deaton, A. Haefele, F.N. Castellano, Organometallics 32 (2013) 3819−3829.
[68] S.E. Brown-Xu, M.S.J. Kelley, K.A. Fransted, A. Chakraborty, G.C. Schatz, F.N. Castellano, L.X. Chen, J. Phys. Chem. A 120 (2016) 543−550.
[69] K. Haldrup, A.O. Dohn, M.L. Shelby, Michael W. Mara, A.B. Stickrath, M.R. Harpham, J. Huang, X. Zhang, K.B. Møller, A. Chakraborty, F.N. Castellano, D.M. Tiede, L.X. Chen, J. Phys. Chem. A 120 (2016) 7475−7483.
[70] R.W. Hartsock, W. Zhang, M.G. Hill, B. Sabat, K.J. Gaffney, J. Phys. Chem. A 115 (2011) 2920–2926.
[71] R.M. van der Veen, C.J. Milne, A. El Nahhas, F.A. Lima, V.-T. Pham, J. Best, J.A. Weinstein, C.N. Borca, R. Abela, C. Bressler, M. Chergui, Angew. Chem. Int. Ed. 48 (2009) 2711 –2714.
[72] K. Haldrup, T. Harlang, M. Christensen, A. Dohn, T.B. van Driel, K.S. Kjær, N. Harrit, J. Vibenholt, L. Guerin, M. Wulff, M.M. Nielsen, Inorg. Chem. 50 (2011) 9329–9336.
[73] R.M. van der Veen, J.J. Kas, C.J. Milne, V.-T. Pham, A. El Nahhas, F.A. Lima, D.A. Vithanage, J.J. Rehr, R. Abela, M. Chergui, Phys. Chem. Chem. Phys. 12 (2010) 5551–5561.
[74] A.O. Dohn, E.O. Jónsson, K.S. Kjær, T.B. van Driel, M.M. Nielsen, K.W. Jacobsen, N.E. Henriksen, K.B. Møller, J. Phys. Chem. Lett. 5 (2014) 2414−2418.
[75] T.B. van Driel, K.S. Kjær, R.W. Hartsock, A.O. Dohn, T. Harlang, M. Chollet, M. Christensen, W. Gawelda, N.E. Henriksen, J.G. Kim, K. Haldrup, K.H. Kim, H. Ihee, J. Kim, H. Lemke, Z. Sun, V. Sundström, W. Zhang, D. Zhu, K.B. Møller, M.M. Nielsen, K.J. Gaffney, Nat. Comm. 7 (2016) 13678.
[76] A.O. Dohn, Direct Dynamics Simulations of $Ir_2(dimen)_4^{2+}$, Transient Changes in Molecular Geometries and How to Model Them: Simulating Chemical Reactions of Metal Complexes in Solution to Explore Dynamics, Solvation, Coherence, and the Link to Experiment, Springer International Publishing, Cham, 2015, pp. 75-97.
[77] S. Grimme, J.-P. Djukic, Inorg. Chem. 50 (2011) 2619–2628.
[78] R.M. van der Veen, C.J. Milne, V.-T. Phama, A. El Nahhas, J.A. Weinstein, J. Best, C.N. Borca, C. Bressler, M. Chergui, Chimia 62 (2008) 287–290.
[79] T.J. Penfold, B.F.E. Curchod, I. Tavernelli, R. Abela, U. Rothlisberger, M. Chergui, Phys. Chem. Chem. Phys. 14 (2012) 9444–9450.
[80] G.I. Gellene, D.M. Roundhill, J. Phys. Chem. A 106 (2002) 7617-7620.
[81] A.J. Bridgeman, G. Cavigliasso, L.R. Ireland, J. Rothery, J. Chem. Soc., Dalton Trans. (2001) 2095–2108.
[82] S. Záliš, H.B. Gray, A. Vlček Jr., Inorg. Chem., submitted (2017).
[83] P. Coppens, J. Benedict, M. Messerschmidt, I. Novozhilova, T. Graber, Y.-S. Chen, I. Vorontsov, S. Scheinsa, S.-L. Zhenga, Acta Crystallogr., Sect. A 66 (2010) 179-188.
[84] M. Kalbáč, S. Záliš, A. Vlček Jr., unpublished results.
[85] R. Monni, G. Auböck, K.M. Lange, D. Kinschel, H.B. Gray, A. Vlček, M. Chergui, Chem. Phys. Lett., submitted (2017).
[86] S.F. Rice, H.B. Gray, J. Am. Chem. Soc. 103 (1981) 1593-1595.
[87] Q. Kong, K.S. Kjaer, K. Haldrup, S.P.A. Sauer, T.B. van Driel, M. Christensen, M.M. Nielsen, M. Wulff, Chem. Phys. 393 (2012) 117–122.

[88] A.G. Sykes, K.R. Mann, J. Am. Chem. Soc. 112 (1990) 7247-7254.
[89] Y.C. Lam, PhD Dissertation, PhD Dissertation, California Institute of Technology, 2015.
[90] I. Novozhilova, A.V. Volkov, P. Coppens, J. Am. Chem. Soc. 125 (2003) 1079-1087.
[91] S.R. Stoyanov, J.M. Villegas, D.P. Rillema, J. Phys. Chem. B 108 (2004) 12175-12180.
[92] I.V. Novozhilova, A.V. Volkov, P. Coppens, Inorg. Chem. 43 (2004) 2299-2307.
[93] H. Isci, W.R. Mason, Inorg. Chem. 24 (1985) 1761-1765.
[94] D.C. Smith, V.M. Miskowski, W.R. Mason, H.B. Gray, J. Am. Chem. Soc. 112 (1990) 3759-3767.
[95] M. Christensen, K. Haldrup, K. Bechgaard, R. Feidenhans'l, Q. Kong, M. Cammarata, M. Lo Russo, M. Wulff, N. Harrit, N. M.M., J. Am. Chem. Soc. 131 (2009) 502–508.
[96] S. Grimme, J. Antony, S. Ehrlich, H. Krieg, J. Chem. Phys. 132 (2010) 154104.
[97] L.S. Fox, J.L. Marshall, H.B. Gray, J.R. Winkler, J. Am. Chem. Soc. 109 (1987) 6901-6902.
[98] J.K. Nagle, D.M. Roundhill, Chemtracts-Inorg. Chem. 4 (1992) 141-155.
[99] R.F. Dallinger, V.M. Miskowski, H.B. Gray, W.H. Woodruff, J. Am. Chem. Soc. 103 (1981) 1595-1596.
[100] C.D. Kim, S. Pillet, G. Wu, W.K. Fullagar, P. Coppens, Acta Crystallogr. A 58 (2002) 133-137.
[101] Y. Ozawa, M. Terashima, M. Mitsumi, K. Toriumi, N. Yasuda, H. Uekusa, Y. Ohashi, Chem. Lett. 32 (2003) 62-63.
[102] P. Coppens, O. Gerlits, I.I. Vorontsov, A.Y. Kovalevsky, Y.-S. Chen, T. Graber, M. Gembicky, I.V. Novozhilova, Chem. Commun. (2004) 2144–2145.
[103] S.K. Doorn, K.C. Gordon, R.B. Dyer, W.H. Woodruff, Inorg. Chem. 31 (1992) 2284-2285.
[104] Q.-J. Pan, H.-G. Fu, H.-T. Yu, H.-X. Zhang, Inorg. Chem. 45 (2006) 8729-8735.
[105] J.V. Caspar, H.B. Gray, J. Am. Chem. Soc. 106 (1984) 3029-3030.
[106] A. Cannizzo, F. van Mourik, W. Gawelda, G. Zgrablic, C. Bressler, M. Chergui, Angew. Chem. Int. Ed. 45 (2006) 3174-3176.
[107] A. Cannizzo, A.M. Blanco-Rodríguez, A. Nahhas, J. Šebera, S. Záliš, A. Vlček, Jr., M. Chergui, J. Am. Chem. Soc. 130 (2008) 8967-8974.
[108] C. Consani, M. Mirabelle Prémont-Schwarz, A. El Nahhas, C. Bressler, F. van Mourik, A. Cannizzo, M. Chergui, Angew. Chem. Int. Ed. 48 (2009) 7184 –7187.
[109] A. El Nahhas, C. Consani, A.M. Blanco-Rodríguez, K.M. Lancaster, O. Braem, A. Cannizzo, M. Towrie, I.P. Clark, S. Záliš, M. Chergui, A. Vlček, Jr., Inorg. Chem. 50 (2011) 2932–2943.
[110] O. Bräm, A. Cannizzo, M. Chergui, Phys. Chem. Chem. Phys. 14 (2012) 7934–7937.
[111] O. Bräm, F. Messina, A.M. El-Zohry, A. Cannizzo, M. Chergui, Chem. Phys. 393 (2012) 51–57.
[112] A.M. Blanco-Rodríguez, H. Kvapilová, J. Sýkora, M. Towrie, C. Nervi, G. Volpi, S. Záliš, A. Vlček, Jr., J. Am. Chem. Soc. 136 (2014) 5963–5973.
[113] M. van Veenendaal, J. Chang, A.J. Fedro, Phys. Rev. Lett. 104 (2010) 067401.
[114] J.N. Schrauben, K.L. Dillman, W.F. Beck, J.K. McCusker, Chem. Sci. 1 (2010) 405–410.
[115] I. Iwakura, T. Kobayashi, A. Yabushita, Inorg. Chem. 48 (2009) 3523-3528.
[116] G.J. Hedley, A. Ruseckas, I.D.W. Samuel, Chem. Phys. Lett. 450 (2008) 292–296.
[117] F. Messina, E. Pomarico, M. Silatani, E. Baranoff, M. Chergui, J. Phys. Chem. Lett. 6 (2015) 4475−4480.
[118] Z.A. Siddique, Y. Yamamoto, T. Ohno, K. Nozaki, Inorg. Chem. 42 (2003) 6366-6378.
[119] Z.A. Siddique, T. Ohno, K. Nozaki, Inorg. Chem. 43 (2004) 663-673.
[120] R. Englman, J. Jortner, Mol. Phys. 18 (1970) 145-164.
[121] Y.C. Lam, H.B. Gray, J.R. Winkler, J. Phys. Chem. A 120 (2016) 7671−7676.
[122] S. Oberneder, G. Gliemann, J. Phys. Chem. 93 (1989) 4487-4489.
[123] S.J. Milder, Inorg. Chem. 24 (1985) 3376-3378.
[124] M. Fetterolf, A.E. Friedman, Y.-Y. Yang, H. Offen, P.C. Ford, J. Phys. Chem. 92 (1988) 3760-3763.
[125] S.J. Milder, D.S. Kliger, L.G. Butler, H.B. Gray, J. Phys. Chem. 90 (1986) 5567-5570.
[126] A.A. Rachford, F.N. Castellano, Inorg. Chem. 48 (2009) 10865–10867.

[127] S. Huang, B. Yang, J. Zhong, H. Zhang, Synth. Met. 205 (2015) 222-227.
[128] K. Saito, Y. Nakao, K. Umakoshi, S. Sakaki, Inorg. Chem. 49 (2010) 8977–8985.
[129] V.M. Miskowski, T.P. Smith, T.M. Loehr, H.B. Gray, J. Am. Chem. Soc. 107 (1985) 7925-7934.
[130] C.-M. Che, W.P. Schaefer, H.B. Gray, M.K. Dickson, P.B. Stein, D.M. Roundhill, J. Am. Chem. Soc. 104 (1982) 4253-4255.
[131] G.S. Rodman, A.J. Bard, Inorg. Chem. 29 (1990) 4699-4702.
[132] D.C. Boyd, G.S. Rodman, K.R. Mann, J. Am. Chem. Soc. 108 (1986) 1779-1784.
[133] C.-M. Che, S.J. Atherton, L.G. Butler, H.B. Gray, J. Am. Chem. Soc. 106 (1984) 5143–5145.
[134] S.C. Cheng, C.A. Blaine, M.G. Hill, K.R. Mann, Inorg. Chem. 35 (1996) 7704-7708.
[135] J.P. Perdew, K. Burke, M. Ernzerhof, Phys. Rev. Lett. 77 (1996) 3865-3868.
[136] C. Adamo, V. Barone, J. Chem. Phys. 110 (1999) 6158-6170.
[137] S. Grimme, J. Antony, S. Ehrlich, H. Krieg, J. Chem. Phys. 132 (2010) 154104.
[138] J. Tomasi, B. Mennucci, R. Cammi, Chem. Rev. 105 (2005) 2999-3093.
[139] R. Ditchfield, W.J. Hehre, J.A. Pople, J. Chem. Phys. 54 (1971) 724-728.
[140] K. Raghavachari, J.S. Binkley, R. Seeger, J.A. Pople, J. Chem. Phys. 72 (1980) 650-654.
[141] A.D. McLean, G.S. Chandler, J. Chem. Phys. 72 (1980) 5639-5648.
[142] D. Andrae, U. Häussermann, M. Dolg, H. Stoll, H. Preuss, Theor. Chim. Acta 77 (1990) 123-141.
[143] J.M.L. Martin, A. Sundermann, J. Chem. Phys. 114 (2001) 3408-3420.
[144] G. Te Velde, F.M. Bickelhaupt, S.J.A. van Gisbergen, C. Fonseca Guerra, E.J. Baerends, J.G. Snijders, T. Ziegler, J. Comput. Chem. 22 (2001) 931-967.

Highlights

• Excitation, reduction, and oxidation strengthen d^8-d^8 metal-metal bonding interactions

• Long-lived singlet and triplet excited states and dual emission are frequent features of d^8-d^8 complexes

• Femtosecond optical excitation triggers coherent motions of the metal-metal unit

• Higher excited states have mixed-spin, with some charge-transfer character

• Two-electron superreduced complexes feature $(p\sigma)^2$ metal-metal bonds combined with electron delocalization over the ligands

Graphical Abstract: